MODELING OF ACOUSTIC WAVES IN PIPES WITH IMPEDANCE WALLS AND DOUBLE ROOTS

By

MATTHEW KELSTEN

A thesis submitted to the

School of Graduate Studies

Rutgers, The State University of New Jersey

in partial fulfillment of the requirements

for the degree of

Master of Science

Graduate Program in Mechanical and Aerospace Engineering

written under the direction of

Dr. Andrew Norris

and approved by

_____

_____

_____

New Brunswick, New Jersey

October, 2018

ABSTRACT OF THE THESIS

Modeling of acoustic waves in pipes with impedance walls and double roots

By MATTHEW KELSTEN

Thesis Director:

Dr. Andrew Norris

Non-Hermitian systems can exhibit exceptional points (EPs) at which modes coalesce. The connection between EPs and acoustic damping goes back to the observation of Cremer (1953) that optimal attenuation in a duct occurs when the two lowest modes have equal complex-valued eigenvalues, although the physical basis for this effect remains unclear. In an attempt to understand Cremer's observation we consider the model cases of a two and three-dimensional waveguide with different impedance conditions on the boundaries. Introductory work delves into the intricacies of waveguide modeling such as solution obtaining methodologies, modal dependencies, phase velocities, group velocities, Green's function solutions, and impedance discontinuity effects. An EP existence condition is derived and explored for both cases. Doing so in this order allows for the determination of the complete set of all possible pairs of passive impedance conditions that give rise to EPs, and from these to select impedances appropriate to a particular frequency band. Numerical and computational simulations are presented to demonstrate modeling legitimacy with the inclusion of some preliminary experimental work for the purpose of establishing experiments to test physically realizable EP behavior. All results point towards promising alternatives and or explanations for large and almost perfect broadband absorption. The theoretical findings are compared to realistic passive impedance values based on models for boundary impedance. These comparisons are discussed to illustrate the feasibility of optimized wall impedances in absorbing sound passing through ducts.

Acknowledgments

First and foremost, I would to to thank my adviser, Dr. Andrew Norris. Throughout both my undergraduate and graduate studies, I have learned more from him than any other educator in my life. Without his willingness to take me on as a student, pursuing my dream of a higher education in the field of engineering would not have been possible. Because of the work we've done together, I have been able to travel to two Acoustical Society of America conferences to present our work and was able to win the Second Best Student Paper Award under the category of Structural Acoustics. I am eternally grateful for the funding, travel opportunities, and insight that he has provided me over the past two years. His ingenuity and patience is rivaled by few.

I would also like to thank the members of the committee: Dr. Jonathan Singer and Dr. Aaron Mazzeo. I've been fortunate enough to have taken the class Analytical Dynamics with Dr. Mazzeo who was incredibly helpful and insightful. I have not had the privilege of taking any class taught by Dr. Singer, however, he is a much respected researcher and I look forward to hearing his structural comments and constructive commentary.

I would like to thank the rest of the faculty and staff member of he Mechanical and Aerospace Engineering Department of Rutgers University. If it wasn't for the undergraduate and graduate programs offered here, I would not be as knowledgeable in the topic of engineering as I am today. I am also grateful for the teaching assistantship opportunities.

I would like to thank Xiaoshi Su and Lucas Lu for their help over the years.

Last but not least, I would like to thank my family and friends for their love and support.

Dedication

For my friends and family.

Table of Contents

List of Tables

List of Figures

Chapter 1
Introduction

Studying the behavior of acoustical waves traveling through a waveguide has been a popular topic of investigation dating back to the 1930's. These solutions typically create a solid foundation from which to build upon for more complicated and applicable problems. For instance, eliminating exhaust noise stemming from internal combustion engines or minimizing air duct noise when considering architectural work are just two relevant topics that depend on fundamental solutions of this sort, as pointed out by Lapin [2]. Morse was one of the orginal pioneers in the field. In 1939 [3] he had delved into the effects of acoustical impedances on wave attenuation within the waveguide. His main findings include that attenuation is higher for wall impedances that exhibit higher elasticity over ones with higher inertial effects, given that they have equal acoustic resistances (real part of the impedance), and that lower order waves typically experience less attenuation than higher order ones. In 1940 [4], Morse looked at the correlating effects between impedance and absorption while comparing his predictions with measured industry standard values. For the time his models showed great accuracy. Shenderov in [5] built upon the models at the time by considering more complicated solutions to the zero eigenvalue mode, also referred to as the fundamental mode. He makes use of a linear solution to the Helmholtz equation and found the specific condition in which this mode can exist outside of a completely rigid-walled waveguide; the condition being that at least one of the walls of the waveguide must have a purely positive imaginary impedance.

All previously mentioned work has been based off of separable solutions to the wave equation, i.e. an infinite amount of distinct modes all contributing to overall acoustic fields which are determined by boundary conditions. However, it was not until Cremer [1] in 1953 when it is unveiled that there exist modes that can be of equal complex value that are completely controlled by wall impedances, commonly referred to as double roots, mode coalescence, or exceptional points (EPs). Within his work, he goes on to claim that EPs are the driving force behind achieving optimal attenuation in waveguides; a very sought after attribute. As time passed, more publications had added to Cremer's findings. Shenderov [6] published his work on deriving EP conditions via non-separable solutions to the Helmholtz equation in addition to extending the phenomena to higher order EPs for both a two and three dimensional pipe. Both Shenderov [6] and Tester [7] present their own derivations to a

corrected Green's function solutions which is quite useful when considering the fact that the classic approach is undefined when EPs are involved.

Despite the numerous publications on the topic, there are questions still left to be answered. It is still unclear how to close the gap between mathematical entities and physically realizable cases in the context of double roots. What is presented in this work will shed light on this topic as we explore not just the existence of EPs themselves, but the effect they have on other well known waveguide parameters. In chapter 2 We will consider both a two and three dimensional pipe with uniform thickness and varying wall impedances where we first work at the general separable solutions in order to provide a solid foundation into the minutiae of classical waveguide modeling. A derivation of EP conditional existence follows suite in chapter 3, similar to that of [6], in an effort to redefine those conditions for the use of a better launching point into the discussion on feasibility. Chapter 4 covers impedance discontinuity modeling techniques in order to look at realistic cases of reflection and transmission trends between EP and non-EP hybrid waveguide systems, all while comparing the performance to traditional energy dissipation techniques in pipes like that of perforated sections [14]. The promising effect EPs have on the overall acoustic pressure fields are highlighted with numerical and simulated results/comparisons in chapter 4. Physical constraints of general impedances are derived in chapter 5 to supplement the discussion of EP feasibility. To bring this work full circle, chapter 5 gives some preliminary experimental research and testing of a custom impedance tube apparatus and is shown to be useful in the future categorizing of realized EP wall impedances. The conclusion can be found in chapter 6.

Chapter 2
Equations for a damped waveguide

2.1 General solution for a 2D waveguide

Consider a two dimensional waveguide with width h depicted in Figure 2.1. The governing equation for the behavior of sound in any waveguide is the wave equation,

$$\frac{\partial^2 p}{\partial t^2} - c^2 \bigtriangledown^2 p = 0 \tag{2.1}$$

where p is the acoustic pressure and c is the acoustic wave speed. One may arrive at the wave equation by considering a continuum model approximation of the fluid medium. A pressure differential across a fluid element will cause it to undergo volumetric changes and translation. Interrelating both of these effects will result in equation (2.1). The solution of (2.1) by means of separation of variables is

$$p(x, y, t) = \sum \phi_n(y)\, e^{i(\gamma_n k x - \omega t)}, \tag{2.2}$$

where $k = \omega/c$ and γ_n is a separation constant for the n^{th} mode. The dependence $e^{i(\gamma_n k x - \omega t)}$ is omitted but understood in the remainder. The modal dependence in the $y-$direction is

$$\phi_n(y) = A_n \cos \beta_n \frac{y}{h} + B_n \sin \beta_n \frac{y}{h}, \tag{2.3}$$

where β_n is the n^{th} eigenvalue, related to the wavenumber in the $x-$direction by

$$\gamma_n = \sqrt{1 - \left(\frac{\beta_n}{kh}\right)^2}. \tag{2.4}$$

The upper and lower walls of the waveguide are characterized by the effective impedances $Z_{1\text{eff}}$ and $Z_{2\text{eff}}$. We assume they are complex valued, of the form

$$Z_{\text{eff}} = -i\omega M + \zeta + \frac{iK}{\omega}. \tag{2.5}$$

The effective impedance takes into consideration the superposition of inertial effects (M = mass per unit area), elastic effects (K = elasticity per unit area), and the dissipation ζ. Note that we

will assume the impedance is locally reacting. Applying continuity of velocity at both walls in conjunction with the momentum equation, $v = \frac{1}{i\omega\rho}\frac{\partial p}{\partial x}$, generates the boundary conditions

$$p = -\alpha_1 h \frac{\partial p}{\partial y}\Big|_{y=\frac{h}{2}}, \qquad p = \alpha_2 h \frac{\partial p}{\partial y}\Big|_{y=-\frac{h}{2}}, \tag{2.6}$$

with

$$\alpha_j = \frac{Z_{j\text{eff}}}{-i\omega\rho h} = \frac{1}{\rho h}\Big(M_j + \frac{i\zeta_j}{\omega} - \frac{K_j}{\omega^2}\Big) \quad \text{for} \quad j = 1, 2. \tag{2.7}$$

Note Equations (2.3) and (2.6) give

$$\begin{pmatrix} \cos\frac{\beta_n}{2} - \alpha_1\beta_n \sin\frac{\beta_n}{2} & \sin\frac{\beta_n}{2} + \alpha_1\beta_n\cos\frac{\beta_n}{2} \\ \\ \cos\frac{\beta_n}{2} - \alpha_2\beta_n \sin\frac{\beta_n}{2} & -\sin\frac{\beta_n}{2} - \alpha_2\beta_n\cos\frac{\beta_n}{2} \end{pmatrix} \begin{pmatrix} A_n \\ \\ B_n \end{pmatrix} = \begin{pmatrix} 0 \\ \\ 0 \end{pmatrix} \tag{2.8}$$

and setting the determinant to zero yields the first eigenvalue relation [5]

$$F_1(\beta) \equiv (1 - \alpha_1\alpha_2\beta_n^2)\sin\beta_n + (\alpha_1 + \alpha_2)\beta_n\cos\beta_n = 0. \tag{2.9}$$

For later use we define solutions that satisfy the boundary conditions on $y = h/2$ and $y = -h/2$, respectively,

$$\begin{aligned} \phi_n^{(1)}(y) &= -\sin\Big(\beta_n\frac{y}{h} - \frac{\beta_n}{2}\Big) + \alpha_1\beta_n\cos\Big(\beta_n\frac{y}{h} - \frac{\beta_n}{2}\Big), \\ \phi_n^{(2)}(y) &= \sin\Big(\beta_n\frac{y}{h} + \frac{\beta_n}{2}\Big) + \alpha_2\beta_n\cos\Big(\beta_n\frac{y}{h} + \frac{\beta_n}{2}\Big). \end{aligned} \tag{2.10}$$

Note either $\phi_n^{(1)}(y)$ or $\phi_n^{(2)}(y)$ are functional for (2.2), the only difference lies in which wall impedance is preferably used. With that being understood, we will continue with $\phi_n^{(2)}(y)$ where the superscript will be omitted.

2.1.1 Symmetric waveguide

If the wall properties are identical ($\alpha_1 = \alpha_2 = \alpha$) then eq. (2.9) reduces to

$$\Big(\cos\frac{\beta_n}{2} - \alpha\beta_n\sin\frac{\beta_n}{2}\Big)\Big(\sin\frac{\beta_n}{2} + \alpha\beta_n\cos\frac{\beta_n}{2}\Big) = 0. \tag{2.11}$$

The parenthetical terms in equation (2.11) correspond respectively to symmetric ($\phi_n(y) = \phi_n(-y)$) and antisymmetric ($\phi_n(y) = -\phi_n(-y)$) modes, i.e.

$$\tan\frac{\beta_n}{2} = \begin{cases} \frac{1}{\alpha\beta_n}, & \text{symmetric}, \\ -\alpha\beta_n, & \text{antisymmetric}. \end{cases} \tag{2.12}$$

This can be rewritten

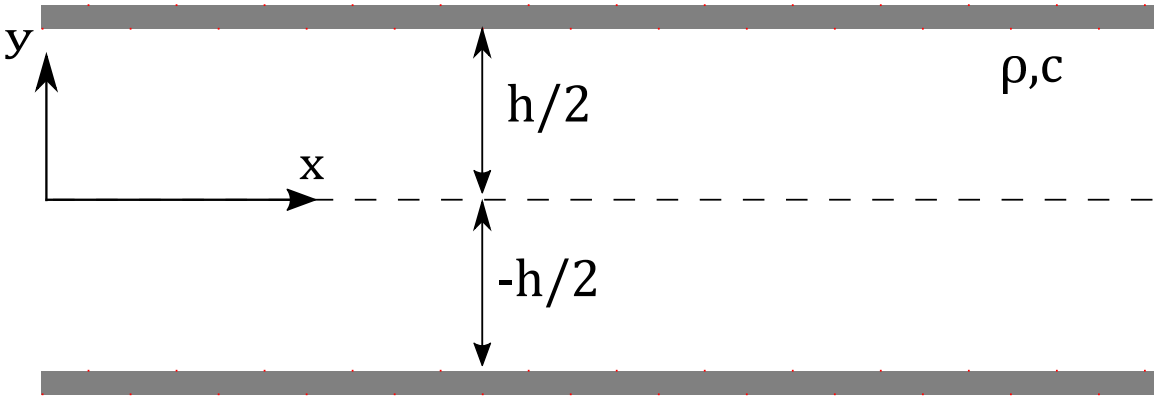

Figure 2.1: Waveguide sketch with width h. ρ, c are the fluid medium density and wave speed respectively.

$$\beta_n + 2\tan^{-1}\alpha\beta_n = \begin{cases} (2n-1)\pi, & \text{symmetric, } \alpha\beta_n \geq 0 \\ (2n-3)\pi, & \text{symmetric, } \alpha\beta_n < 0 \end{cases} \quad \text{for } n = 1, 2, \ldots.$$
$$\beta_n + 2\tan^{-1}\alpha\beta_n = \begin{cases} 2n\pi, & \text{antisymmetric, } \alpha\beta_n \geq 0 \\ 2(n-1)\pi, & \text{antisymmetric, } \alpha\beta_n \leq 0 \end{cases} \quad \text{for } n = 1, 2, \ldots. \tag{2.13}$$

Hence, for $n \geq 2$,

$$\beta_n \approx \begin{cases} \left(2n - 1 - \frac{2}{\pi}\tan^{-1}\left((2n-1)\pi\alpha\right)\right)\pi, & \text{symmetric,} \\ \left(2n - \frac{2}{\pi}\tan^{-1}\left(2n\pi\alpha\right)\right)\pi, & \text{antisymmetric,} \end{cases} \quad \text{for } \alpha\beta_n \geq 0, \tag{2.14}$$

$$\beta_n \approx \begin{cases} \left(2n - 3 - \frac{2}{\pi}\tan^{-1}\left((2n-1)\pi\alpha\right)\right)\pi, & \text{symmetric,} \\ \left(2(n-1) - \frac{2}{\pi}\tan^{-1}\left(2(n-1)\pi\alpha\right)\right)\pi, & \text{antisymmetric,} \end{cases} \quad \text{for } \alpha\beta_n < 0. \tag{2.15}$$

with the approximation improving with n.

Now consider the possibility of complex modal values. Start by assuming that the impedances of both loseless walls are identical, i.e. $\alpha_1 = \alpha_2$, and $\beta_n = -i|\beta_n|$. The negative sign is present for the fact that we are looking for mode values strictly in the fourth quadrant of the complex plane. As mentioned in [5], this conclusion can be drawn by considering the imaginary part of the relationship $\gamma_n^2 = 1 - (\beta_n/kh)^2$, yielding

$$\Re\gamma_n \Im\gamma_n = -(kh)^{-2}\Re\beta_n \Im\beta_n. \tag{2.16}$$

Since $\Re\gamma_n$ and $\Im\gamma_n$ must both be positive in order to have only attenuating and forward-traveling waves, Eq. (2.16) implies that $\Re\beta_n$ and $\Im\beta_n$ must be of opposite signs. It is also important to note that changing the sign of the root, whether real or complex, does not produce new unique solutions.

All of these points lead to the conclusion that maintaining a focus on the fourth quadrant for roots is sufficient. Equation (2.12) then becomes

$$\tanh\frac{|\beta_n|}{2} = \begin{cases} -\frac{1}{\alpha|\beta_n|}, & \text{symmetric,} \\ -\alpha|\beta_n|, & \text{antisymmetric.} \end{cases} \tag{2.17}$$

Due to the nature of $\tanh(|\beta_n|/2)$, these complex modal values will only exist for $\alpha < 0$, and in turn, only be present for waveguides with elastically dominant impedances ($K/w^2 > M$). For a graphical representation, see Figure 2.2. Note that for a value of $|\alpha| > 0.5$ only one intersection point, and therefore only symmetric modes, exists while two intersection points will occur for $|\alpha| < 0.5$, i.e. both symmetric and antisymmetric modes can exist. It is easier to reconcile this effect by observing the derivatives with respect to $|\beta_n|$ of $\tanh(|\beta_n|/2)$ and $-\alpha|\beta_n|$ at $|\beta_n| = 0$. In order for these two functions to meet, the slope of $-\alpha|\beta_n|$ must be less than that of $\tanh(|\beta_n|/2)$, or in inequality form: $\alpha > -0.5$. Figure 2.3 demonstrates the behavior of the complex roots of equation (2.17) in tandem with the first real antisymmetric branch corresponding to the modes associated with the second term of equation (2.11). It also introduces the non-dimensional frequency

$$\Omega = \frac{\omega h}{c}. \tag{2.18}$$

This notation will be used in upcoming equations and figures.

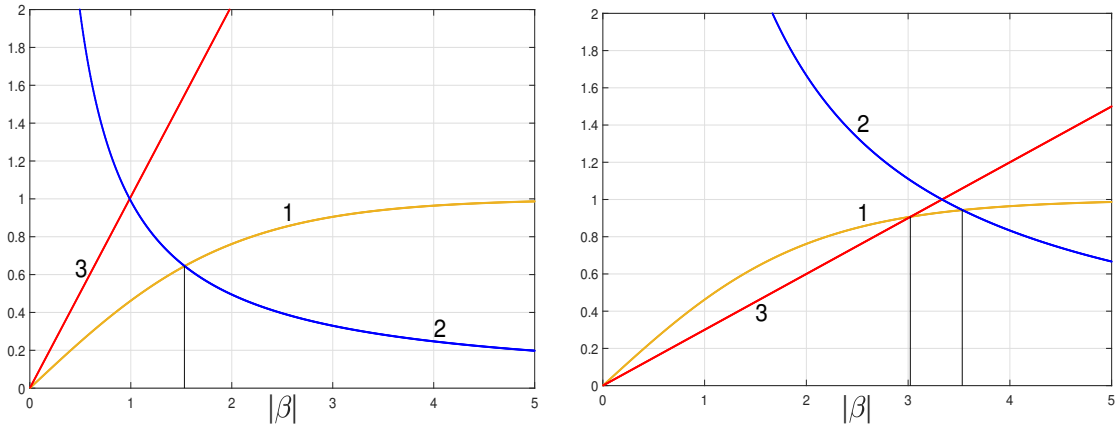

(a) An example with $|\alpha| > 0.5$, specifically $|\alpha| = 1$.

(b) An example with $|\alpha| < 0.5$, specifically $|\alpha| = 0.3$.

Figure 2.2: Curves 1, 2, and 3 represent $\tanh(|\beta|/2)$, $1/(-\alpha|\beta|)$, and $-\alpha|\beta|$ respectively. Black lines signify intersection points, see Eq. (2.16).

Inspection of Figure 2.3 leads to a better understanding of complex modal behavior. Both the symmetric and antisymmetric complex branches tend to be asymptotic to $\Omega = 10$ ($\omega = 1$) for the set of parameters given in figure 2.3. Considering that this frequency corresponds to this particular waveguide being acoustically soft ($\alpha = 0$), the trend supports the claim that complex modes will

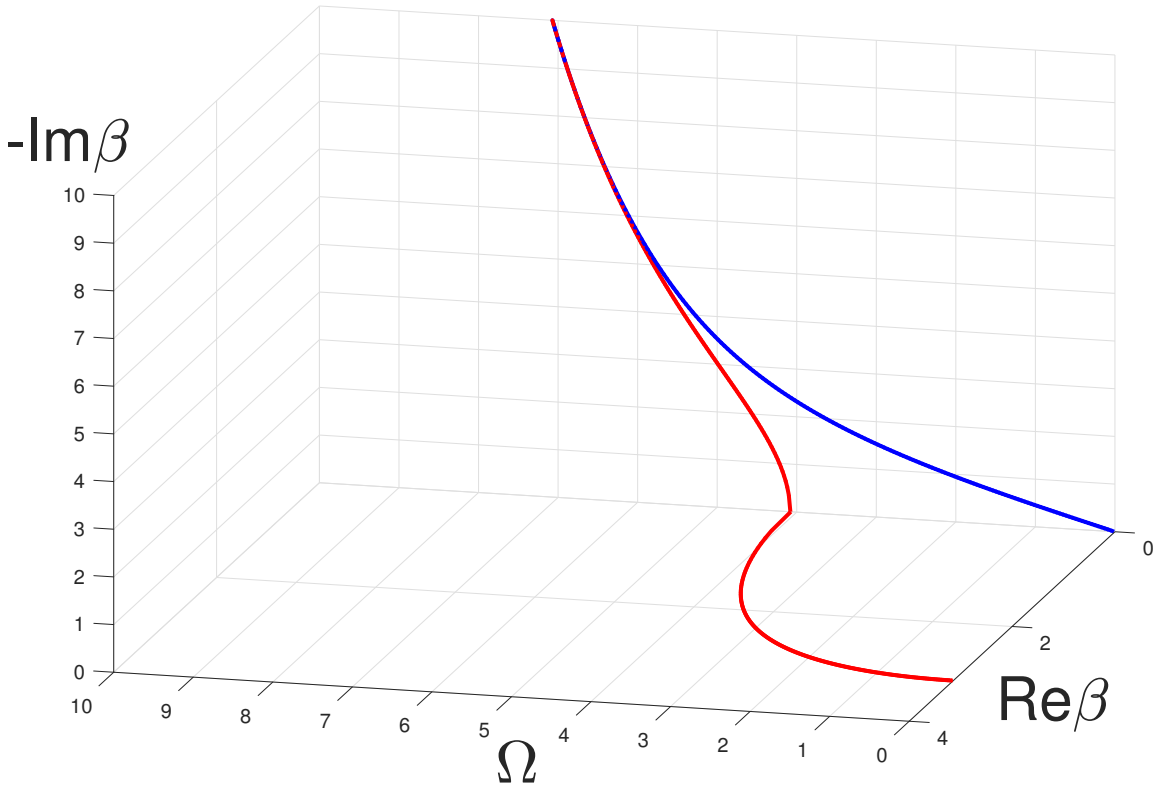

Figure 2.3: Depiction of the first real antisymmetric mode branch (red, $\Omega - \Re\beta$ plane) in addition to both the symmetric (blue) and antisymmetric (red, $\Omega - \Im\beta$ plane) complex mode branches of a lossless waveguide. Parameters include $K = M = \rho = 1, h = 10$. A similar figure is found in Shenderov [5].

only exist for waveguides experiencing higher elasticity than inertial effects. Also note at which point the antisymmetric branch begins is also when both types of roots start to exist, suggesting that it is at this frequency where $|\alpha|$ becomes less than a half.

2.2 Phase and Group Speeds

2.2.1 Phase Speed

Phase speed is defined as the rate at which each phase propagates along the waveguide. Consider the phase of a given mode to be $\gamma_n kx - \omega t$, where γ_n is the separation constant, as mentioned before, that also pertains to the wave number of that particular mode. By differentiating the modal phase with respect to time and setting it equal to zero we arrive at

$$v_n^{ph} = \frac{c}{\sqrt{1 - \left(\frac{\beta_n}{\Omega}\right)^2}}. \tag{2.19}$$

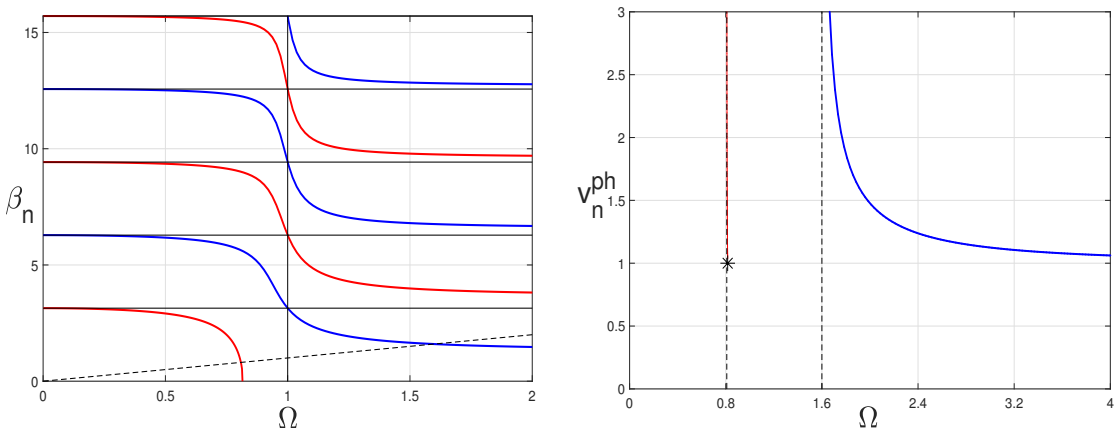

(a) Dotted line illustrates cutoff frequency trend.

(b) Dotted lines and * signify cutoff frequencies and zeroth mode, respectively.

Figure 2.4: Lossless mode shapes (a) and their respective phase speeds (b) for $K = M = \rho = h = 1$. K and M values chosen to have acoustically soft impedances ($\alpha = 0$) at $\Omega = 1$. Red and blue signify antisymmetric and symmetric modes, respectively.

Figure 2.4(b) refers to the phase speeds of each corresponding mode branch illustrated in figure 2.4(a). Notice how there are only two speed branches present for this range of frequencies. This is due to the fact that all other modes lead to evanescent, or exponentially decaying, solutions because they are all above the cutoff frequency. the cutoff frequency is simply defined as the frequency at which point γ_n becomes complex for a set of given parameters. Revisiting the example of figure 2.4 with $K = M = \rho = h = 1$, this is illustrated by the relation $\Omega_{\text{cutoff}} = \omega_{\text{cutoff}} = \beta_n$, where Ω is the non-dimensional frequency. A graphical representation of the cutoff frequency is illustrated by the dashed lines in figures 2.4(a) and 2.4(b). Changing certain parameters, such as the width of the waveguide etc., will change the cutoff and allow for more modes to propagate. The aforementioned method was used to achieve propagating phase speeds for a multitude of modes by increasing the width of the guide and subsequently changing the cutoff relation to $\omega_{\text{cutoff}} = \beta_n/10$ (or $\Omega_{\text{cutoff}} = \beta_n$), seen in figures 2.5(a) and 2.5(b). Note that a change in waveguide dimensions only does not lead to a change in the non-dimensional cutoff frequency relation, but still allows for more propagating modes.

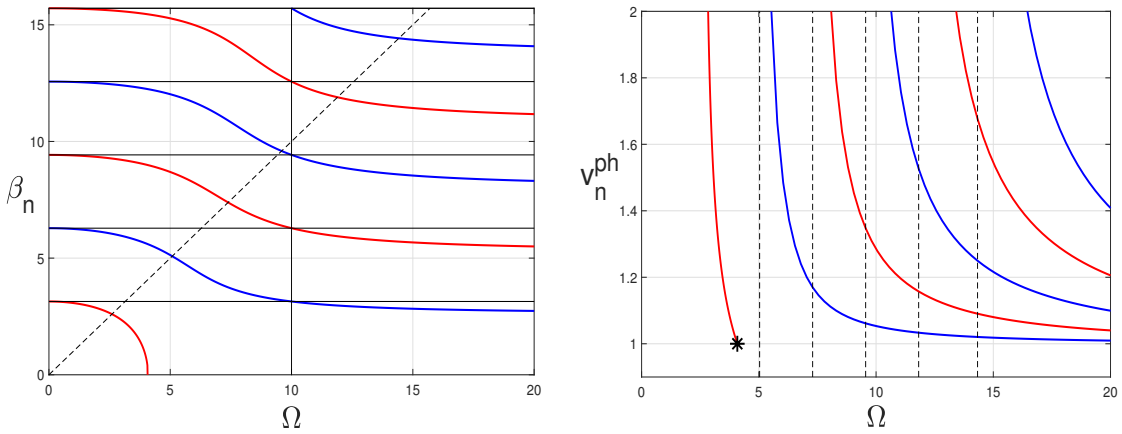

(a) Dotted line illustrates cutoff frequency trend.

(b) Dotted lines and * signify cutoff frequencies and zeroth mode, respectively.

Figure 2.5: Lossless mode shapes (a) and their respective phase speeds (b) for $K = M = \rho = 1, h = 10$. K and M values chosen to have acoustically soft impedances ($\alpha = 0$) at $\Omega = 10$. Red and blue signify antisymmetric and symmetric modes respectively.

2.2.2 Group Speed

Another characteristic of wave motion is known as the group speed, or the speed of the wave packet composed of multiple individual waves that contribute to the overall waveform. Group speed will be defined as $v_n^{gr} = \frac{d\omega}{dk_x}$ where $k_x = k\gamma_n$. Both group and phase speeds will not be one in the same as long as there is dispersion present. Thus,

$$v_n^{gr} = \frac{c\sqrt{1 - \left(\frac{\beta_n}{\Omega}\right)^2}}{1 - \left(\frac{\beta_n}{\Omega}\right)^2 \Gamma} \tag{2.20a}$$

$$\text{where} \quad \Gamma = \frac{\omega}{\beta_n}\frac{d\beta_n}{d\omega} = \frac{\alpha - \frac{1}{\rho h}(M + \frac{Kh^2}{\Omega^2 c^2})}{\alpha + \frac{1}{2} + \frac{1}{2}(\alpha\beta_n)^2}. \tag{2.20b}$$

The expression for Γ follows by using Eq. (2.11) to get

$$\frac{d\beta_n}{d\alpha} = -\beta_n\left(\alpha + \frac{1}{2} + \frac{1}{2}(\alpha\beta_n)^2\right)^{-1} \tag{2.21}$$

for both symmetric and antisymmetric modes, and then using Eq. (2.7) for $d\alpha/d\omega$. It is important to note that all group speeds, regardless of which modal branch they originated from, are asymptotic to the acoustic medium speed c. The peculiar value of the zeroth mode's group speed will be discussed in the next section.

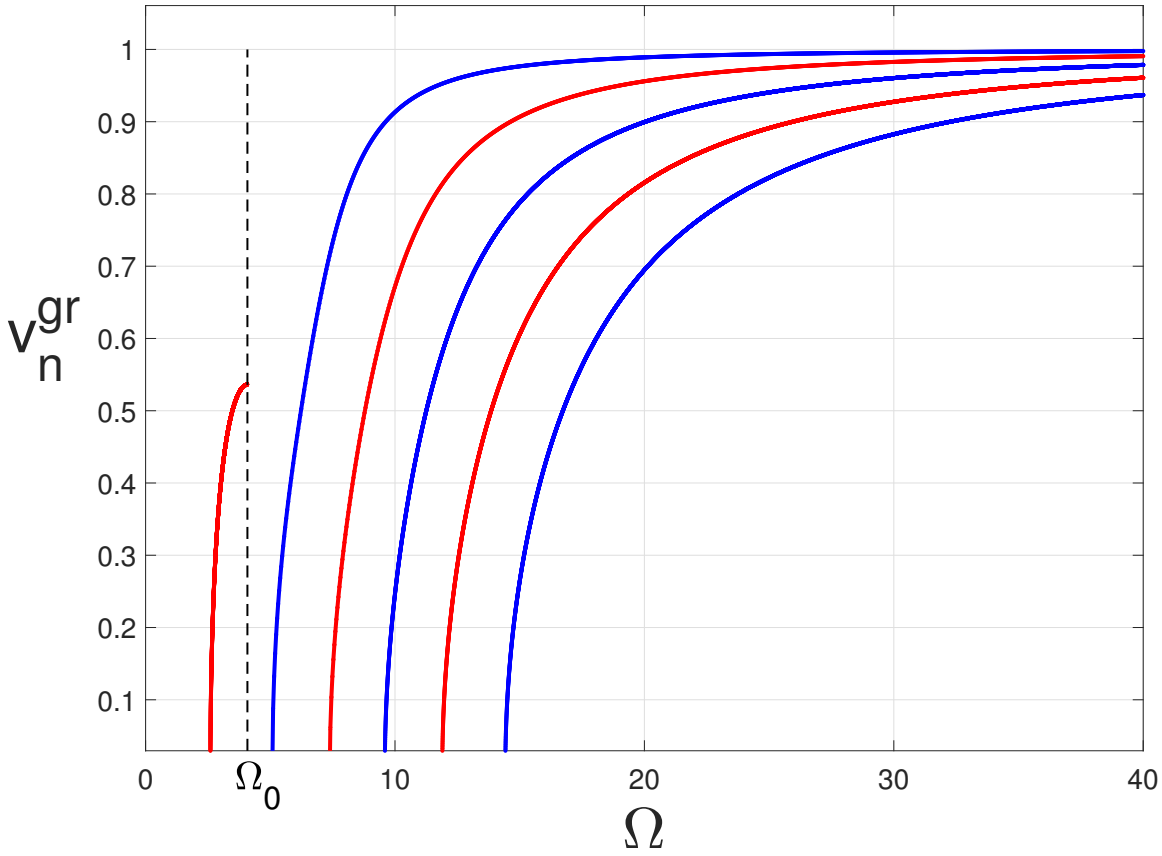

Figure 2.6: Group speeds corresponding to lossless mode shape branches of 2.5(a). Red and blue signify antisymmetric and symmetric modes, respectively. Dotted line representative of the non-dimensional frequency ($\Omega_0 = \frac{\omega_0 h}{c}$) correlating to $\alpha = -1/2$ e.g. the zeroth mode. $c = 1$.

Perturbation: zeroth mode

Perturbation theory is applied to the zeroth mode ($\beta = 0$) of the first antisymmetric mode branch for better understanding of exact roots. Consider the antisymmetric part of equation (2.11) expanded into its Taylor series. We arrive at

$$\Big(\frac{\beta_n}{2} - \frac{\beta_n^3}{48} + \frac{\beta_n^5}{120 * 32} + \dots\Big) + \alpha\beta_n\Big(1 - \frac{\beta_n^2}{8} + \frac{\beta_n^4}{24 * 16} + \dots\Big) = 0 \tag{2.22}$$

Factoring out a β_n and applying a perturbation around $\alpha = -1/2$, specifically $\alpha = -\frac{1}{2} + \epsilon$, generates the perturbed polynomial

$$\epsilon + \beta_n^2\Big(\frac{1}{24} - \frac{\epsilon}{8}\Big) + \beta_n^4\Big(\frac{-1}{960} + \frac{\epsilon}{384}\Big) + \dots = 0. \tag{2.23}$$

Substituting in $\beta_n = \epsilon^p x$ with $p = 1/2$ and grouping the coefficients together by powers of ϵ produces the second order perturbation roots around zero

$$\beta_{01}^2 \approx \beta_{02}^2 \approx -\epsilon\Big(24 + \frac{288}{5}\epsilon + \frac{3492}{25}\epsilon^2 + \frac{15768}{125}\epsilon^3 + \dots\Big). \tag{2.24}$$

Utilizing the perturbation series in conjunction with the group speed relations will provide some insight on the group speed value of the zeroth mode. We start with substituting in equation (2.24) into equation (2.20) in order to achieve a closed form expression of the perturbed group speeds. After some amount of algebra we arrive at

$$v_0^{gr}(\epsilon) = \frac{c\sqrt{1+\frac{24\epsilon}{\Omega_0^2}(1+\frac{12}{5}\epsilon+\ldots)}}{1+\frac{12}{\Omega_0^2}\big(1+\frac{2M}{\rho h}-12\epsilon\big)(1+\frac{24}{5}\epsilon+\ldots)} \tag{2.25}$$

where Ω_0 is the Ω value tied to $\alpha = -1/2$ for a set of given parameters. More specifically, as ϵ goes to zero the perturbed group speed of a lossless waveguide simplifies to

$$v_0^{gr}(0) = \frac{c}{1+\frac{24Kh}{\kappa\Omega_0^4}} \qquad \text{by using} \qquad \Omega_0^2 = \frac{Kh}{(\frac{1}{2}+\frac{M}{\rho h})\kappa}. \tag{2.26}$$

The $\kappa = \rho c^2$ term in equation (2.26) is known as the bulk modulus of the fluid medium. We can test the accuracy of equation (2.26) by plugging in the parameters used for 2.5(a) which include $K = M = \rho = c = 1, h = 10$. A value of $v_0^{gr}(0) \approx 0.536$ is obtained when this is performed which closely agrees with the result seen in figure 2.6. Now with equation (2.26) in hand, it is possible to start considering and evaluating conditions relevant to maximizing this fundamental value. The physical limitations considered here is that the group speed cannot be greater than that of the free medium speed c. With this in mind, it is advantageous to study how this zeroth mode group speed varies with changing parameters, more specifically how it increases approaching the free medium speed. It is obvious that v_0^{gr} approaches c as the denominator in (2.26) approaches unity, which can be accomplished in different ways. The most evident of those being the wall elasticity measurement K, going to infinity, or in other words the impedance of the waveguide becoming acoustically hard. An increase in waveguide width will also have a similar effect.

2.3 General solution for a 3D axisymmetric waveguide

A similar approach is taken in order to solve that of a uniform cylindrical waveguides with constant radius b which is axisymmetric, or there are no geometric nor impedance changes with respect to the circumferential direction. The Helmholtz equation with cylindrical coordinates and the axisymmetric assumption is

$$(\bigtriangledown^2 + k^2)\Psi(r,\theta,z) = 0 \text{ with } \bigtriangledown^2 = \big(\frac{\partial^2}{\partial r^2} + \frac{1}{r}\frac{\partial}{\partial r} + \frac{\partial^2}{\partial x^2}\big), \tag{2.27}$$

where r, x are the radial and axial directions respectively. k is once again the wavenumber of the medium. Separation of variables, $\Psi = R(r)X(x)$, generates the ordinary differential equations

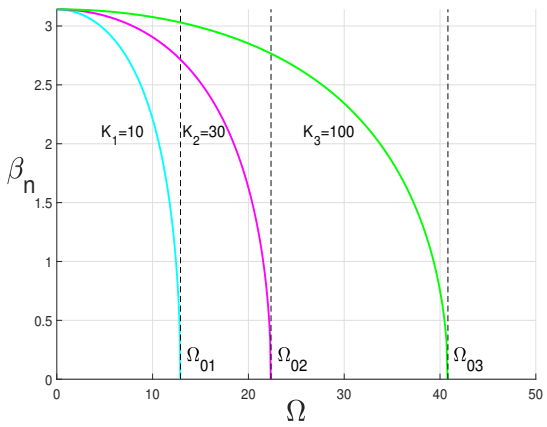

(a) Mode shapes for first antisymmetric branch with varying K.

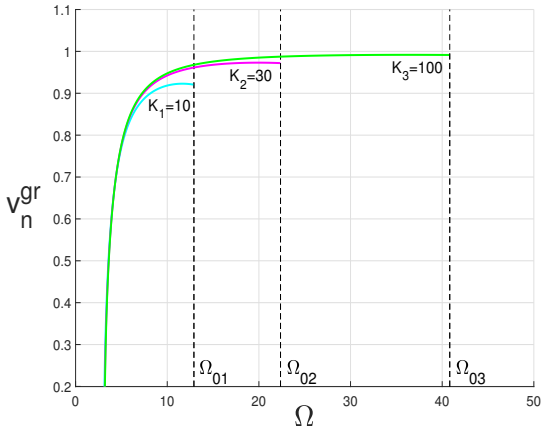

(b) Group speeds of mode branches in 2.7(a), $c = 1$.

Figure 2.7: Lossless mode shapes (a) and their respective group speeds (b) for $M = \rho = 1, h = 10$, and varying K. Dashed lines suggest location of non-dimensional frequency $\Omega_{0j} = \frac{\omega_{0j} h}{c}$, for $j = 1, 2, 3$, that lead to $\alpha = -1/2$ for each value of K. All branches are color coordinated.

(ODEs)

$$\frac{1}{R}\frac{d^2R}{dr^2} + \frac{1}{rR}\frac{dR}{dr} + k^2 + \frac{1}{X}\frac{d^2X}{dx^2} = 0 \rightarrow \begin{cases} \frac{1}{X}\frac{d^2X}{dx^2} = -k^2\gamma^2, \\ r^2\frac{d^2R}{dr^2} + r\frac{dR}{dr} + r^2\left(\frac{\beta}{b}\right)^2 R = 0, \ \left(\frac{\beta}{b}\right) = k^2 - k^2\gamma^2. \end{cases} \tag{2.28}$$

It is easily seen that the top ODE solution works out to be

$$X(x) = Ae^{ik\gamma x} \tag{2.29}$$

for forward traveling waves. The bottom ODE takes the form of Bessel's equation which has the known solution

$$R(r) = CJ_0(\beta r/b) + DN_0(\beta r/b), \tag{2.30}$$

where J_0 and N_0 are the Bessel functions of the first ad second kind of order zero (attributed to the axisymmetric assumption). the unknown coefficient D will be zero so the overall solution remains bounded at $r = 0$. Application of the velocity continuity boundary condition at the wall, $\frac{\partial \Psi}{\partial r} = \frac{ik\rho c}{Z}\Psi\Big|_{r=b} = -\frac{1}{\alpha b}\Psi\Big|_{r=b}$ (a direct consequence of the momentum equation $v = \frac{1}{i\omega\rho}\frac{\partial p}{\partial x}$ as seen in the 2D case), bears the eigenvalue relation

$$F_1(\beta) = J_0(\beta) - \alpha\beta J_1(\beta) = 0, \ \alpha = \frac{Z}{-i\omega\rho b}. \tag{2.31}$$

The modes given by (2.31) are dictated by the same second or fourth quadrant in the complex plane restriction as the modes for the 2D case. Equation (2.29)-(2.31) gives all eigenfunctions Ψ_n:

$$\Psi_n = \psi_n(r)e^{ik\gamma_n x} = A_n J_0(\beta_n r/b)e^{ik\gamma_n x}. \tag{2.32}$$

Note that the coefficient A_n is not the same as in (2.29) and γ_n is given in (2.28). The overall pressure fields now being defined as

$$p(x, r, t) = \sum \psi_n(r) e^{i(k\gamma x - \omega t)}. \tag{2.33}$$

Chapter 3

Non-Separable Solutions to the Helmholtz Equation and exceptional points

3.1 2D waveguide

In all of the previous findings above, a strictly separable solution to the Helmholtz equation was assumed; however, this will not always be the case. As mentioned by Shenderov [6], there exist possible solutions that require additional specifications on the waveguide impedances; once these are met, they will start to contribute to the overall acoustic fields. For better comprehension let us refer back to our original work, but consider the existence of less intuitive solutions. The original problem had equation (2.9) to find the eigenvalues which have their own respective spatial solution

$$s_n(x,y) = \phi_n(y)e^{i\gamma_n kx}, \tag{3.1}$$

where each eigenfunction ϕ_n is a valid solution for the Helmholtz equation. Let us assess a new function $t_q(x,y,\beta_q)$ described by Shenderov in [6] and defined by

$$t_q(x,y,\beta_q) = \frac{\partial s_q(x,y,\beta_q)}{\partial \beta_q} = \Big[\frac{\partial \phi_q(y,\beta_q)}{\partial \beta_q} - \frac{ix\beta_q}{kh^2\gamma_q}\phi_q(y,\beta_q)\Big]e^{i\gamma_q kx}, \tag{3.2}$$

where the subscript q refers to the mode β_q and its subsequent modal conditions only. It is easy to see that the term containing ϕ_q already satisfies the boundary conditions presented in (2.6), so the next logical move is to find at what values of β_q does $\frac{\partial \phi_q(y,\beta_q)}{\partial \beta_q}$ meet them as well. For instance, the explicit form becomes

$$\frac{\partial \phi_q(y,\beta_q)}{\partial \beta_q} = \Big(\frac{y}{h}+\frac{1}{2}\Big)\Big(\cos\Big(\beta_q\frac{y}{h}+\frac{\beta_q}{2}\Big) - \alpha_2\beta_q\sin\Big(\beta_q\frac{y}{h}+\frac{\beta_q}{2}\Big)\Big) + \alpha_2\cos\Big(\beta_q\frac{y}{h}+\frac{\beta_q}{2}\Big). \tag{3.3}$$

Application of equation (3.3) into the boundary conditions of (2.6) implies that a non-separable solution of the form $t_q(x,y,\beta_q)$ can occur only if β_q is a root of (2.9) and $F_2(\beta_q)$:

$$\begin{aligned} F_1(\beta_q) &= (1-\alpha_1\alpha_2\beta_n^2)\sin\beta_q + (\alpha_1+\alpha_2)\beta_q\cos\beta_q = 0, \\ F_2(\beta_q) &= \beta_q\sin\beta_q\Big(2\alpha_1\alpha_2+\alpha_1+\alpha_2\Big) + \cos\beta_q\Big(\alpha_1\alpha_2\beta_q^2-\alpha_1-\alpha_2-1\Big) = 0. \end{aligned} \tag{3.4}$$

β_q is commonly referred to as a double root. More specifically, the smallest mode (in terms of absolute value) to satisfy (3.4) will cause the first two adjacent symmetric modes to coalesce. The

second smallest mode satisfying (3.4) will cause the first and second antisymmetric adjacent modes to coalesce and so on. Note that "order" of modes will be treated as low to high. The two former instances are demonstrated in figure 3.1. However, in terms of absorption it will always be more beneficial to have the first two symmetric modes coalesce for they are the least attenuated. This attribute will become more clear in the coming sections under chapter 4. Again, the subscripts q

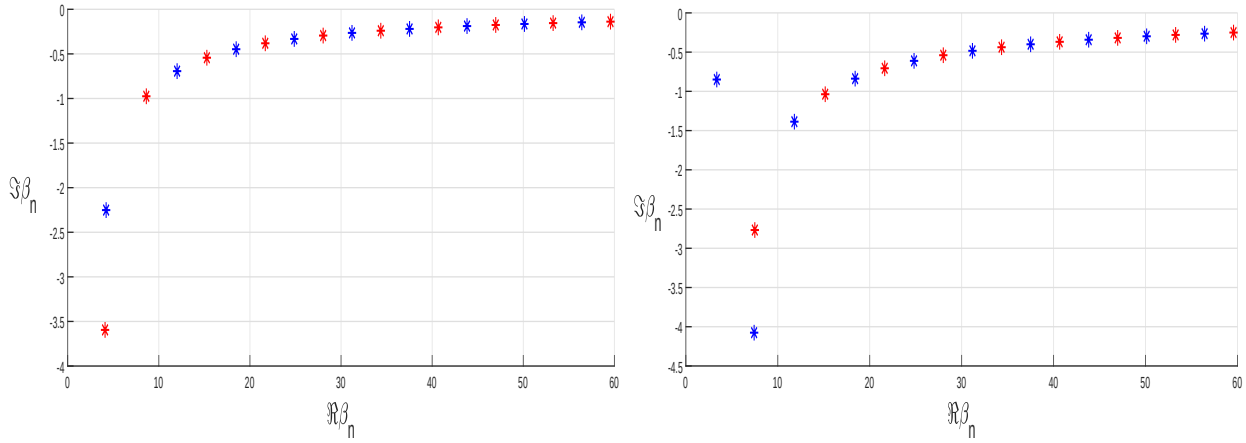

Figure 3.1: First handful of modes for a 2D waveguide with EP impedance walls corresponding to the first symmetric 3.1(a) and antisymmetric 3.1(b) double roots at 1000 Hz and $h = 0.3m$.

specifies modes that satisfy both equations of (3.4). It is important to note that F_2 is the derivative with respect to the mode of F_1, $dF_1/d\beta$. Eliminating the trigonometric functions yields an algebraic relation

$$\alpha_1^2\alpha_2^2\beta_q^4 + \Big((\alpha_1+\alpha_2+2)\alpha_1\alpha_2 + (\alpha_1-\alpha_2)^2\Big)\beta_q^2 + \alpha_1 + \alpha_2 + 1 = 0. \tag{3.5}$$

While this can be solved to yield β_q in terms of the impedances, we find it more constructive to consider the impedances as dependent on β_q. Following Shenderov [6], eliminating α_1 between the two relations (3.4) implies $H(\alpha_2, \beta_q) = 0$ where

$$H(\alpha_2, \beta_q) \equiv \frac{1}{2}\Big(1 + 2\alpha_2 \sin^2\beta_q + \beta_q^2\alpha_2^2 + (\beta_q^2\alpha_2^2 - 1)\frac{\sin 2\beta_q}{2\beta_q}\Big). \tag{3.6}$$

$H(\alpha_2, \beta_q)$ is related to the integral of ϕ_q^2, i.e. the orthogonality relation:

$$H(\alpha_2, \beta_q) = \frac{1}{h}\int_{-h/2}^{h/2} \phi_q^2(y)dy. \tag{3.7}$$

The equally symmetric dependence of α_1 and α_2 in (3.4) implies that $H(\alpha_1)$ is zero at the double root. Hence the conditions (3.4) can be replaced by a pair of identities each involving only one impedance:

$$H(\alpha_1, \beta_q) = 0 \quad \text{and} \quad H(\alpha_2, \beta_q) = 0. \tag{3.8}$$

Note that

$$H(\alpha,\beta)=0 \quad \text{if} \quad \alpha=\frac{\frac{\sin 2\beta}{2\beta}-1}{\sin^2\beta\pm\sqrt{\sin^2\beta-\beta^2}}. \tag{3.9}$$

As previously stated, (2.16) showed that physical solutions for β_q must lie in the second or fourth quadrants. We restrict attention to double root values in the fourth quadrant. Numerical experiments then show that the root with the + sign[1] almost always yields an α with non-negative imaginary part, consistent with a passive impedance condition[2]. The exception being when $\Re\beta_q$ is exactly zero. The root with the − sign yields a passive impedance for some values of β. We can therefore work backwards in a sense, and consider some value of β_q and then define the impedances by the two roots:

$$\alpha_n\equiv\frac{\frac{\sin 2\beta_q}{2\beta_q}-1}{\sin^2\beta_q-(-1)^n\left(\sin^2\beta_q-\beta_q^2\right)^{1/2}},\quad n=1,\,2. \tag{3.10}$$

Any choice of β_q gives a passive α_1 as long as $\Re\beta_q>0$. Numerical experiments indicate that there are no passive solutions for α_2 if $-\Im\beta_q<C$ and $\Re\beta_q>0$, where $C\approx 1.105824$. For larger values of $-\Im\beta_q$ it is possible to obtain two passive but distinct values for the wall impedances.

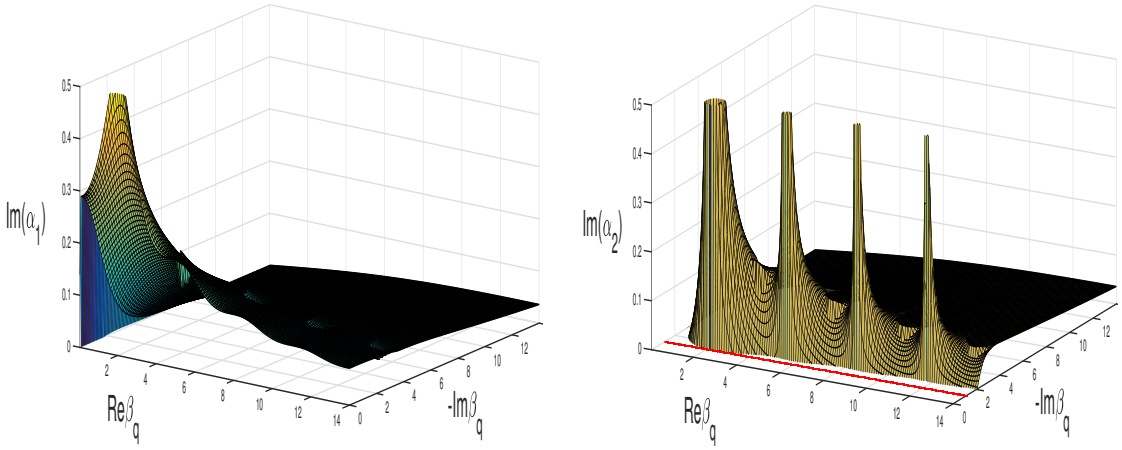

Figure 3.2: Contour figures of passive α_1 and α_2 for a range of $\beta_q=\Re\beta_q-i\Im\beta_q$ values. The red line in (b) represents the boundary $\Im\beta_q=C\approx 1.105824$.

We must interpret the above in terms of the known limiting cases: one or both walls acoustically hard or soft and equal wall impedances. The symmetric waveguide case is simply when the square root term in (3.10) is zero, i.e.

$$\sin\beta_q=\mp\beta_q,\qquad \alpha_1=\alpha_2=\frac{-1}{1\mp\cos\beta_q}, \tag{3.11}$$

[1] We assume the usual branch cut for the square root along the negative real axis such that the real part of the square root is non-negative.

[2] A passive impedance is one that takes away energy, as opposed to an active impedance which supplies energy from an exterior source. They are defined by the sign of the real part of the impedance Z, or equivalently, by the imaginary part of α. The signs are positive for passive impedances, and negative for active ones.

where the $-(+)$ corresponds to symmetric (antisymmetric) mode shapes. The roots of Eq. (3.11) are discussed in Appendix A.. Now imagine a waveguide in which the lower wall was acoustically rigid, i.e. $|\alpha_2| = \infty$. In order for that to be true, the denominator in equation (3.10) must go to zero, giving us the modal condition $\sin 2\beta_q = -2\beta_q$. Substitution into equation (3.10) and some manipulation shows the necessary impedance of the other wall for these double roots to occur in this scenario. Hence,

$$\sin 2\beta_q = -2\beta_q, \quad \alpha_1 = \frac{-2}{1-\cos 2\beta_q}, \quad 1/\alpha_2 = 0. \tag{3.12}$$

A slightly different method can be helpful in determining the results for $\alpha_1 = 0$, or the upper wall being acoustically soft. Consider the numerator in equation (3.10) approaching zero by letting $\frac{\sin 2\beta_q}{2\beta_q} - 1 = \frac{\epsilon}{\beta_q}$ for $\epsilon \ll 1$ and taking the limit. Substitution into equation (3.10) and some algebra produces $\alpha_2 = \epsilon\beta_q^{-1}[\sin^2\beta_q - (\sin^2\beta_q + \epsilon\cot\beta_q + O(\epsilon^2))]^{-1}$, which implies, in the limit that

$$\sin 2\beta_q = 2\beta_q, \quad \alpha_2 = \frac{-2}{1+\cos 2\beta_q}, \quad \alpha_1 = 0. \tag{3.13}$$

Note that for the acoustically hard or soft cases, a reverse methodology where the opposite α is fixed to explicitly solve for β_q and the remaining α will provide the same β_q relation but only trivial α pairs ($\alpha_1 = \alpha_2 = \infty$ or $\alpha_1 = \alpha_2 = 0$). Comparison of Eqs. (3.11), (3.12) and (3.13) shows, as noted by [6], that the values of β_q for the waveguide with one face soft or hard are equal to one half of the corresponding values for the symmetric waveguide, and the associated impedances are twice the impedances of the symmetric waveguide. Figure 3.3 is the result of a refined interpolation method that successfully mimics the boundary between passive and non-passive α_2 values that will satisfy the double root condition. The corresponding value of α_1 is given in (3.10). Since we are only considering passive α_2, figure 3.3 graphically illustrates the real and imaginary mode pairs that are of any significance to the discussion (above the black line) while highlighting the cases of (3.11)-(3.13). It is important to note that both the acoustically hard and acoustically soft cases lie directly on this boundary suggesting that they are, in a way, limiting cases.

The black curve in Figure 3.3(a) is where α_2 is real valued. Using Eq. (3.10), the values of β_q on the boundary curve satisfy

$$\alpha_2^2\beta_q^2\big(1 + \frac{\sin 2\beta_q}{2\beta_q}\big) + 2\alpha_2\sin^2\beta_q + \big(1 - \frac{\sin 2\beta_q}{2\beta_q}\big) = 0. \tag{3.14}$$

This can be written

$$2\beta_q + \sin 2\theta - \sin 2(\beta_q + \theta) = 0 \quad \text{where } \theta = \tan^{-1}(\alpha_2\beta_q). \tag{3.15}$$

Note that Eqs. (3.12) and (3.13) are recovered when $\alpha_2 = 0$ ($\theta = 0$) and $\alpha_2 = \infty$ ($\theta = \frac{\pi}{2}$),

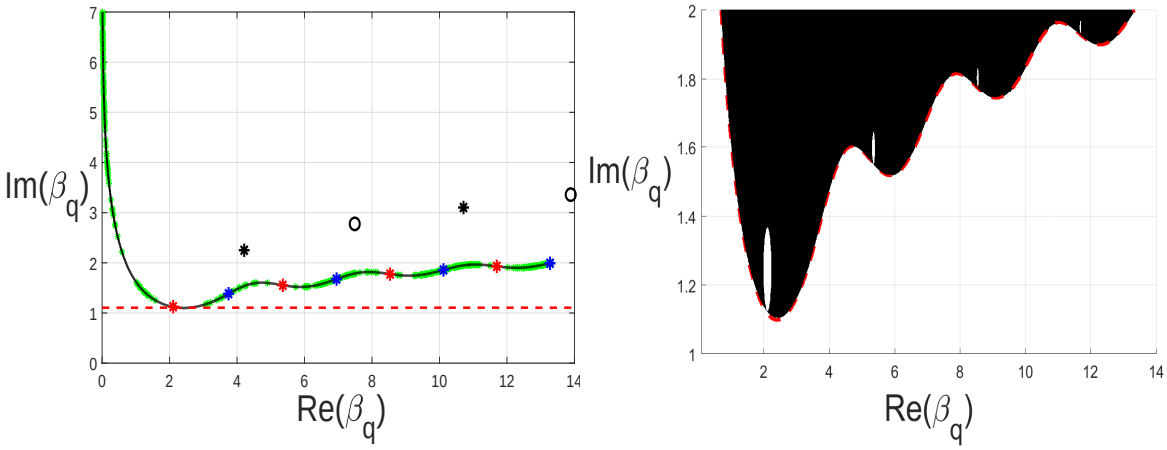

(b) Overlay comparison between interpolated boundary and actual contour boundary.

Figure 3.3: The black curve is the interpolation of the passive α_2 boundary presented in Fig. 3.2(b). Every α_2 point above this curve corresponds to a passive pair of impedances that give rise to a double root: the corresponding value of α_1 is given by Eq. (3.10). The specific points are defined as follows: red, blue and black are for numerical approximations of acoustically hard ($|\alpha_2| = \infty$), acoustically soft ($\alpha_2 = 0$), and symmetrical waveguide ($\alpha_1 = \alpha_2$) solutions, respectively. Symmetric and antisymmetric mode types differentiated by "*" and "o" symbols. Red dashed line marks $-\Im\beta_q \approx 1.105824$. The Green points are those for which $\Im\alpha_2 \approx 0$ and were used to generate the boundary curve.

respectively. Differentiation of Eq. (3.14) yields

$$\frac{d\beta_q}{d\alpha_2} = \begin{cases} -\beta_q, & \alpha_2 = 0, \\ 0, & \alpha_2 = \infty. \end{cases} \tag{3.16}$$

This demonstrates that *the globally minimum value of* $-\Im\beta_q$ *corresponds to the first acoustically hard mode* ($\alpha_2 = \infty$). Inspection of figure 3.3 shows an identifiable pattern between the real and imaginary parts of symmetric and antisymmetric double root modes for a symmetric waveguide. Further investigation produced Figure 3.4, the result of an expanded numerical approximation in conjunction with a curve fitting method that models the modes as a two term power equation:

$$\Im\beta_q = 162.3(\Re\beta_q)^{0.005943} - 161.5. \tag{3.17}$$

3.2 3D axisymmetric waveguide

Consider the 3D axisymmetric waveguide introduced in section 2.3. Likewise, non-separable solutions and exceptional points exists for this system as well. Because of its 3D nature, its derivations are more likely to be linked to physically realizable waveguides making it highly serviceable. We could

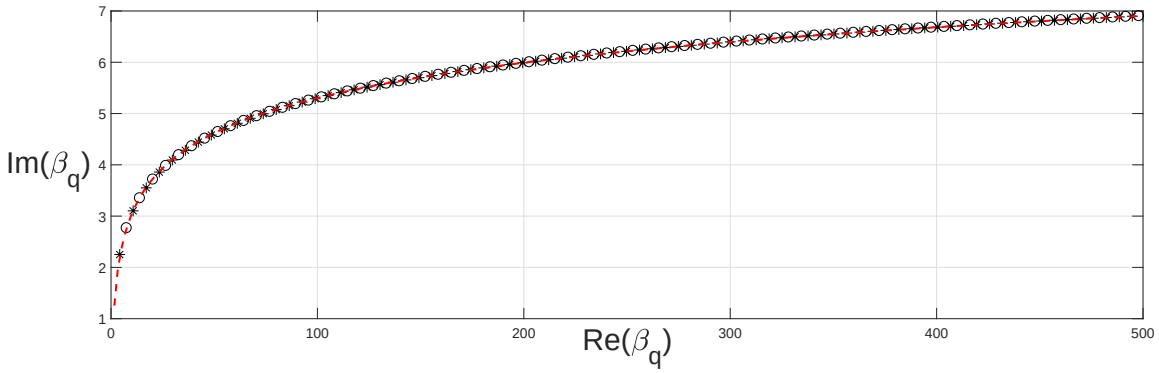

Figure 3.4: Higher order symmetric "*" and antisymmetric "o" double root solutions to the symmetric waveguide case ($\alpha_1 = \alpha_2$). Red dashed line is a result of a numerical curve fitting that takes the form of the two term power equation $\Im\beta_q = 162.3(\Re\beta_q)^{0.005943} - 161.5$.

start with a similar technique as before and introduce a new function

$$g_q(x, r, \beta_q) = \frac{\partial \Psi_q(x, r, \beta_q)}{\partial \beta_q}, \tag{3.18}$$

where Ψ_n is defined by (2.32) and find the secondary modal condition that way. However, a simpler method exists that was highlighted in the previous section, i.e. the non-separable solution and exceptional point condition $F_2(\beta_q)$ is just the derivative of the separable eigenvalue relation with respect to the mode. ergo, taking $dF_1/d\beta$ of equation (2.31) yields

$$F_2(\beta_q) = \frac{dF_1(\beta_q)}{d\beta} = J_1(\beta_q) + \alpha\beta_q J_0(\beta_q) = 0, \tag{3.19}$$

providing a more timely and efficient approach. With F_2 in hand the rest is identical to that of the 2D case; solving for α in F_1 and substitution back into F_2 gives the alternate condition

$$H_q = J_1^2(\beta_q) + J_0^2(\beta_q) = 0, \tag{3.20}$$

where H_q is again related to the orthogonality of the eigenfunction itself

$$\int_0^b \psi_i \psi_j r dr = \begin{cases} = 0, \ i \neq j, \\ = H_i, \ i = j. \end{cases} \tag{3.21}$$

H_q can be rewritten as

$$H_q = J_1^2(\beta_q) + J_0^2(\beta_q) = 0 \rightarrow \Big(J_0(\beta_q) + iJ_1(\beta_q)\Big)\Big((J_0(\beta_q) - iJ_1(\beta_q)\Big) = 0 \tag{3.22}$$

where only one of the parenthetical terms needs to be solved. If β_q is a root of one then so is $-\beta_q, \beta_q^*$, and $-\beta_q^*$; "*" refering to the complex conjugate. Figure 3.5 provides a graphical depiction. Since the fourth quadrant is all that is necessary to completely describe the phenomenon, we will focus

our attention there. This observation provides an ease to numerical mode computations that would normally be tedious. As before, we can instead work backwards and use H_q to find the EP modes which can be utilized to find the corresponding wall impedance,

$$\alpha_{ep} = J_0(\beta_q)/\beta_q J_1(\beta_q), \tag{3.23}$$

found via rearranging F_1.

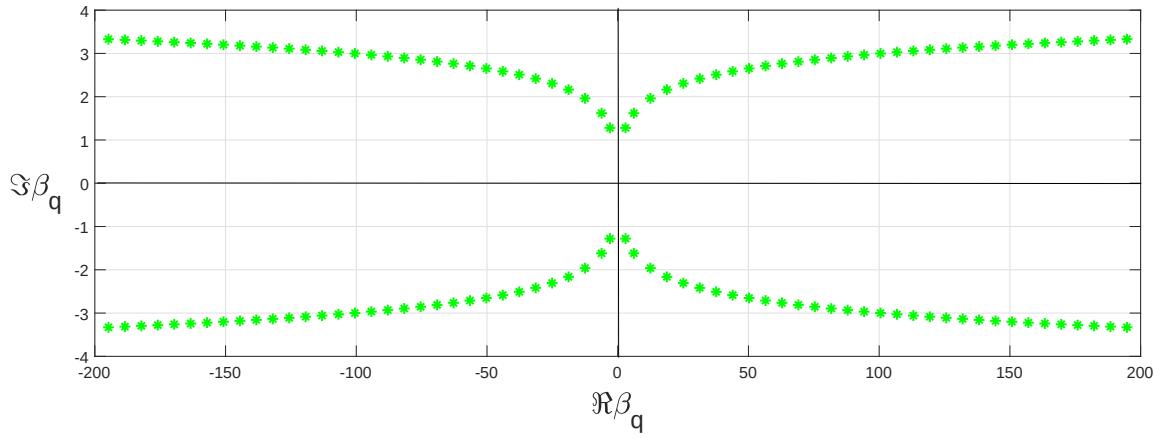

Figure 3.5: EP mode symmetry across four quadrants of the complex plane for a cylindrical axisymmetric waveguide.

3.3 Green's Function for a Two-Dimensional Waveguide around the Presence of Double Roots

Consider a concentrated source located at (x_0,y_0) within the waveguide presented in figure 2.1. In order to solve for the acoustic field generated by this source, the Green's function is introduced which satisfies

$$(\nabla^2 + k^2)G(x, y|x_0, y_0) = -\delta(x - x_0)\delta(y - y_0), \tag{3.24}$$

i.e. the spatial wave equation. A two-dimensional waveguide equipped with impedance boundary conditions that does not exhibit double roots has a well-known Green's function of the form of an infinite series of eigenfunctions,

$$G = \sum_n F_n(x)\phi_n(y). \tag{3.25}$$

$\phi_n(y)$ is the known characteristic eigenfunction above stemming from homogenous Helmholtz equation with impedance boundary conditions. $F_n(x)$ can be obtained via insertion into (3.24), followed

by multiplying both sides by $\phi_n(y)$ and integrating over the waveguide width. After taking into consideration the slope discontinuities at x_0, the results become (see Morse and Ingard [**?**])

$$F_n = \frac{i\phi_n(y_0)}{2kh\gamma_n H_n} e^{ik\gamma_n|x-x_0|}, \qquad G(x,y|x_0,y_0) = \frac{i}{2kh}\sum_n \frac{\phi_n(y)\phi_n(y_0)}{\gamma_n H_n} e^{ik\gamma_n|x-x_0|}. \tag{3.26}$$

Equation (3.26) explicitly shows the inherent problem of using this Green's function when double roots occur. G is undefined when H_n is zero which is an unavoidable property of double root existence. Hence, an updated Green's function that compensates for this behavior is mandatory. Two different approaches to a corrected Green's function are established in [6] and [7]. What is of bigger concern is how the Green's function solution behaves as you approach the double root. In more detail, we will look at the effect of two adjacent modes of similar symmetry approaching one another has on the classic Green's function. Numerical tests of $G(x,y|x_0,y_0)$ in equation (3.26) for a monopole source located at $(0,0)$ suggest that the classic function remains defined regardless of how close these modes become. In fact, figures figures 3.6-3.7 illustrate that the two modes expected to equate at the EP impedance have equal and opposite contributions to the acoustic fields. So although their magnitudes increase to a great extent with respect to the higher modes, they are kept in check by one another.

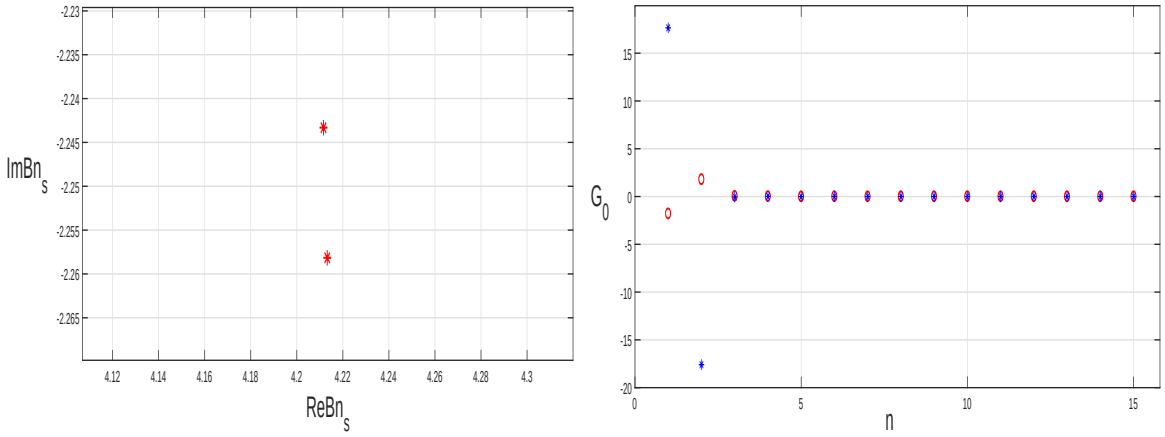

(a) First two symmetric modes of a symmetric waveguide with walls close to that of the first EP impedance.

(b) Modal contributions to the Green's function. Modes approaching one another have equal and opposite effects.

Figure 3.6: 3.6(a) illustrate the first two symmetric modes for a symmetric waveguide with $\alpha = \alpha_{ep}+\epsilon$ where $\epsilon = 10^{-6}i$. 3.6(b) are the Green's function magnitude per mode. Note that the modes close to one another have almost equal and opposite contributions.

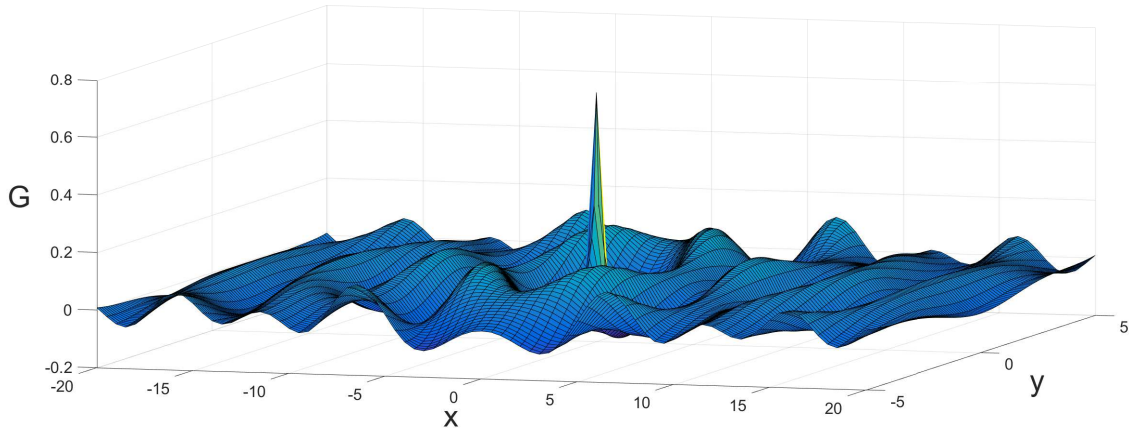

Figure 3.7: Field distribution for a monopole source located at $(0, 0)$ for a symmetric waveguide where the boundary impedances are close to that of the first EP impedance, $\alpha = \alpha_{ep} + 10^{-6}i$.

Chapter 4

Reflection and transmission effects at impedance discontinuities

In this chapter we introduce the concept of impedance discontinuities by considering waveguides with two different wall impedances separated at an interface. When an incoming wave reaches the interface its energy will be both reflected and transmitted similar to that of sound incident on a fluid-solid interface. The purpose of this chapter lies in the inherent reality of discontinuities of this sort in applicable systems. For example, most automotive mufflers will have metal tubing which connects to either expansion chambers for reactive noise control or perforated tubing for dissipative noise control [14]. In addition, these models provide an excellent source of analytical comparisons for different tests performed with an impedance tube. Once models are derived, their validity is discussed following a non-EP into EP hybrid system performance study.

4.1 One discontinuity

A general approach to solving waveguides with wall impedance discontinuities is given. Consider the two-dimensional case of a symmetric waveguide with two unique and different wall impedances separated by a line at $x = 0$. In equation form this looks like

$$Z_1 = Z_2 = \begin{cases} Z_a & x < 0, \\ Z_b, & x > 0. \end{cases} \tag{4.1}$$

Subscripts 1 and 2 correlate to upper wall and lower wall respectively. This impedance discontinuity acts as an interface where reflection and transmission phenomena can occur. In order to solve for said reflection and transmission coefficients, continuity conditions of pressure and velocity at the separation $x = 0$ are applied. These take the form of

$$\begin{aligned} &\phi_{inc}^{(L)}(y)e^{i\gamma_{inc}kx} + \sum_{m=1}^{\infty} R_m\phi_m^{(L)}(y)e^{-i\gamma_m kx} = \sum_{n=1}^{\infty} T_n\phi_n^{(R)}(y)e^{i\theta_n kx} \text{ pressure continuity,} \\ &\gamma_{inc}\phi_{inc}^{(L)}(y)e^{i\gamma_{inc}kx} - \sum_{m=1}^{\infty} \gamma_m R_m\phi_m^{(L)}(y)e^{-i\gamma_m kx} = \sum_{n=1}^{\infty} \theta_n T_n\phi_n^{(R)}(y)e^{i\theta_n kx} \text{ velocity continuity,} \end{aligned} \tag{4.2}$$

where the subscript "inc" is for the incoming wave originating from the left and traveling to the right and R_m (T_n) is the reflection (transmission) coefficient. $\phi_m^{(L)}(y)/\gamma_m$ and $\phi_n^{(R)}(y)/\theta_n$ are the eigenfunction/effective wave number pairs present for the portion of the waveguide with impedance Z_a (Left) and impedance Z_b (Right), respectively. Either can be found by utilizing equation (2.4) in tandem with (2.10) for the specific impedance used on that corresponding side of $x = 0$. If we take both equations of (4.2), multiply them by $\phi_j^{(R)}(y)$, integrate over y and set $x = 0$, we get the following relations:

$$-\sum_{m=1}^{\infty} R_m C_{nm} + T_n H_n = A_n, \qquad \sum_{m=1}^{\infty} \gamma_m R_m C_{nm} + \theta_n T_n H_n = \gamma_{inc} A_n,$$

where

$$C_{nm} = \frac{1}{h}\int_{-h/2}^{h/2} \phi_n^{(R)}(y)\phi_m^{(L)}(y)dy, \qquad H_n = \frac{1}{h}\int_{-h/2}^{h/2} (\phi_n^{(R)}(y))^2 dy, \qquad A_n = \frac{1}{h}\int_{-h/2}^{h/2} \phi_n^{(R)}(y)\phi_{inc}^{(L)}(y)dy. \tag{4.3}$$

Note that orthogonality was used to simplify the transmission series into a single term proportional to H_n, as seen here by

$$\frac{1}{h}\int_{-h/2}^{h/2} \phi_n^{(R)}(y)\phi_j^{(R)}(y)dy = \begin{cases} 0 & n \neq j, \\ H_n & n = j. \end{cases} \tag{4.4}$$

If we consider the incoming wave as a plane wave and the left-portion impedance to be hard, it is easily seen that $A_n = C_{n1}$. The results above can be expressed as a matrix allowing for a conventional computational method to be used in order to solve for the unknown coefficients R_m and T_n as seen below.

$$\begin{bmatrix} -C_{11} & -C_{12} & -C_{13} & \dots & -C_{1M} & H_1 & 0 & 0 & \dots & 0 \\ -C_{21} & -C_{22} & -C_{23} & \dots & -C_{2M} & 0 & H_2 & 0 & \dots & 0 \\ \vdots & \ddots & & & \vdots & \vdots & \ddots & & & \vdots \\ \vdots & & \ddots & & \vdots & \vdots & & \ddots & & \vdots \\ \vdots & & & \ddots & \vdots & \vdots & & & \ddots & \vdots \\ -C_{N1} & -C_{N2} & -C_{N3} & \dots & -C_{NM} & 0 & 0 & 0 & \dots & H_N \end{bmatrix} \begin{pmatrix} R_1 \\ \vdots \\ R_M \\ T_1 \\ \vdots \\ T_N \end{pmatrix} = \begin{pmatrix} A_1 \\ A_2 \\ A_3 \\ \vdots \\ \vdots \\ A_N \end{pmatrix} \tag{4.5}$$

$$\begin{bmatrix} \gamma_1 C_{11} & \gamma C_{12} & \gamma_3 C_{13} & \dots & \gamma_L C_{1M} & H_1\theta_1 & 0 & 0 & \dots & 0 \\ \gamma_1 C_{21} & \gamma_2 C_{22} & \gamma_3 C_{23} & \dots & \gamma_L C_{2M} & 0 & H_2\theta_2 & 0 & \dots & 0 \\ \vdots & \ddots & & & \vdots & \vdots & \ddots & & & \vdots \\ \vdots & & \ddots & & \vdots & \vdots & & \ddots & & \vdots \\ \vdots & & & \ddots & \vdots & \vdots & & & \ddots & \vdots \\ \gamma_1 C_{N1} & \gamma_2 C_{N2} & \gamma_3 C_{N3} & \dots & \gamma_1 C_{NM} & 0 & 0 & 0 & \dots & H_N\theta_N \end{bmatrix} \begin{pmatrix} R_1 \\ \vdots \\ R_M \\ T_1 \\ \vdots \\ T_N \end{pmatrix} = \begin{pmatrix} A_1 \\ A_2 \\ A_3 \\ \vdots \\ \vdots \\ A_N \end{pmatrix} \tag{4.6}$$

Matrix (4.5) and (4.6) can be combined in order to find the $M + N$ unknown coefficients, M and N being the number of terms taken from the left-hand (reflection) and right-hand (transmission) series. The results presented below correspond to an incoming plane wave of unity in a waveguide with acoustically hard walls for $x < 0$ (i.e. $|Z_a| = \infty$) and acoustically soft walls for $x > 0$ (i.e. $Z_b = 0$). The respective eigenfunctions, effective wave numbers, and integrals belonging to equation (4.3) simplify to

$$\begin{aligned} &\phi_m^{(L)}(y) = \cos\Big(\pi(m-1)\Big(\frac{y}{h} + \frac{1}{2}\Big)\Big), \qquad \phi_n^{(R)}(y) = \sin\Big(n\pi\Big(\frac{y}{h} + \frac{1}{2}\Big)\Big), \\ &\gamma_m = \sqrt{1 - \Big(\frac{(m-1)\pi}{kh}\Big)^2}, \qquad \theta_n = \sqrt{1 - \Big(\frac{n\pi}{kh}\Big)^2}, \\ &C_{nm} = \frac{n}{\pi}\Big[\frac{(-1)^{n+m} + 1}{(n+m-1)(n-m+1)}\Big], \qquad H_n = \frac{1}{2}, \qquad A_n = C_{n1}, \\ &\text{where } n, m = 1, 2, 3, \dots. \end{aligned} \tag{4.7}$$

Here, H_n is found via equation (3.6). It is important to note that there exists pairs of n and m such that the denominator of C_{nm} is zero, however, those exact pairs also leave the numerator zero. Thus, we will treat them as defined and equal to zero without sacrificing the accuracy of the approach. Value comparisons between the worked out matrix solution approach against an FEM simulation of the same hard/soft discontinuity taken at a point far away from the interface and at constant width ($h = 0.3$m) are shown in figure 4.1. The greater transmission response compared to that of the incoming unity plane wave, measured at about 560 Hz, can be attributed to a resonance effect with the first eigenfrequency of the soft case. Now that we have established the accuracy and legitimacy of the approach, we can start looking at more interesting cases. Let's consider the the same waveguide with an incoming plane wave of unity, however, we apply an impedance condition

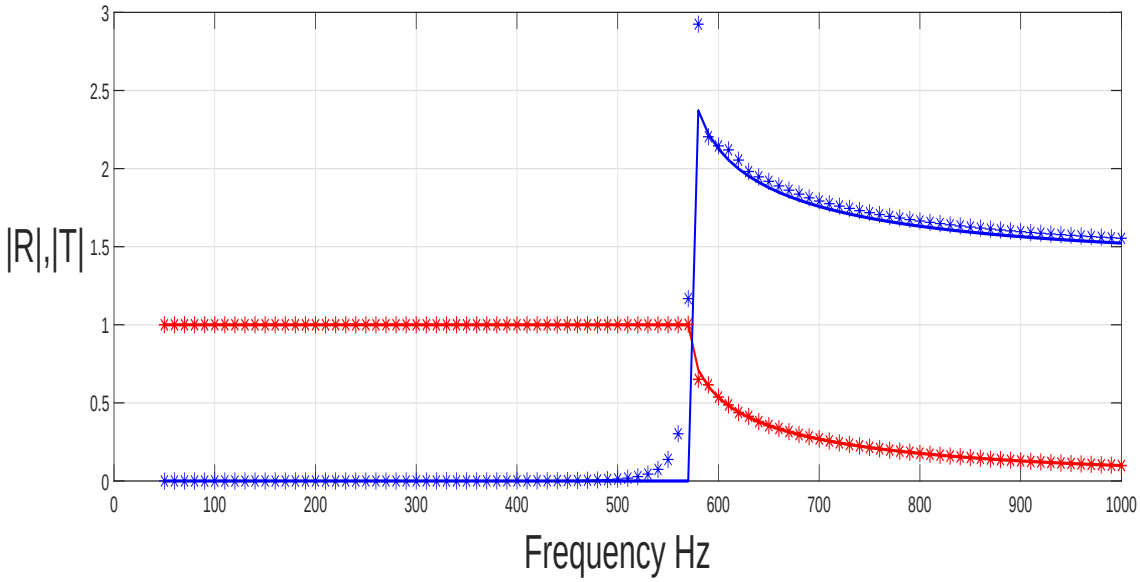

Figure 4.1: Matrix solution compared with a finite elements simulation (COMSOL) for a two-dimensional waveguide with an incident plane wave of unity incoming onto a acoustically hard/soft discontinuity. Reflection is differentiated from transmission by color (red for reflection and blue for transmission) while matrix and FEM methods of solutions are differentiated by lines an "*"'s, respectively. Waveguide width is kept at a constant value of $h = 0.3$m. FEM measurements are taken far from the interface on both sides to avoid inclusion of evanscent modes.

of some complex non-zero α on the right side of the interface. Note that the left side is unchanged and the same left eigenfunction $\phi_m^{(L)}$ and effective wave number γ_m are still applicable. With regards to the new right-side solution, the boundary conditions of equation (2.6) are used for the walls in tandem with equation (2.10) for the eigenfunction. The new solution takes the form of

$$\begin{aligned}
&\phi_m^{(L)}(y) = \cos\Big(\pi(m-1)\Big(\frac{y}{h}+\frac{1}{2}\Big)\Big), \qquad \phi_n^{(R)}(y) = \sin\Big(\beta_n\Big(\frac{y}{h}+\frac{1}{2}\Big)\Big) + \alpha\beta_n\cos\Big(\beta_n\Big(\frac{y}{h}+\frac{1}{2}\Big)\Big),\\
&\gamma_m = \sqrt{1-\Big(\frac{(m-1)\pi}{kh}\Big)^2}, \qquad \theta_n = \sqrt{1-\Big(\frac{\beta_n}{kh}\Big)^2},\\
&C_{nm} = \beta_n\Big[\frac{(-1)^m\cos\beta_n + (-1)^{m-1}\alpha\beta_n\sin\beta_n + 1}{(\beta_n+(m-1)\pi)(\beta_n-(m-1)\pi)}\Big], \qquad A_n = C_{n1},\\
&H_n = \frac{1}{2}\Big(1+2\alpha\sin^2\beta_n + \beta_n^2\alpha^2 + (\beta_n^2\alpha^2-1)\frac{\sin 2\beta_n}{2\beta_n}\Big),
\end{aligned}$$

where β_n is the eigenvalue of the nth mode and $n, m = 1, 2, 3, \ldots$. (4.8)

It is beneficial to verify that the matrix methodology is accomplishing exactly what we set out to do and that is match the pressure and velocity profiles on both sides of the discontinuity. Figure 4.2 and 4.3 suggest just that, demonstrating that the difference of the two profiles approaches zero as we increase the number of modes for the case described in (4.8) using an α close to the first symmetric EP value. Due to the fact that computation times can be lengthy, only 100 and 200

modes are compared, however, these incorporate the aforementioned trends quite sufficiently. To eliminate any remaining doubt about the accuracy of the model, figure 4.4 finishes us off with another side by side comparison of a FEM simulation to the matrix method. Both are solving for the reflected and transmitted pressures at a point 0.5m away from the interface on both sides and on the waveguide centerline. By inspection, it is evident that the agreement is spot on.

$$P_r = \sum_{m=1}^{\infty} R_m \phi_m^{(L)}(y) e^{-i\gamma_m kx}, \qquad P_t = \sum_{n=1}^{\infty} T_n \phi_n^{(R)}(y) e^{i\theta_n kx},$$

$$v_r = -\sum_{m=1}^{\infty} R_m \gamma_m \phi_m^{(L)}(y) e^{-i\gamma_m kx}, \qquad v_t = \sum_{n=1}^{\infty} T_n \theta_n \phi_n^{(R)}(y) e^{i\theta_n kx}.$$

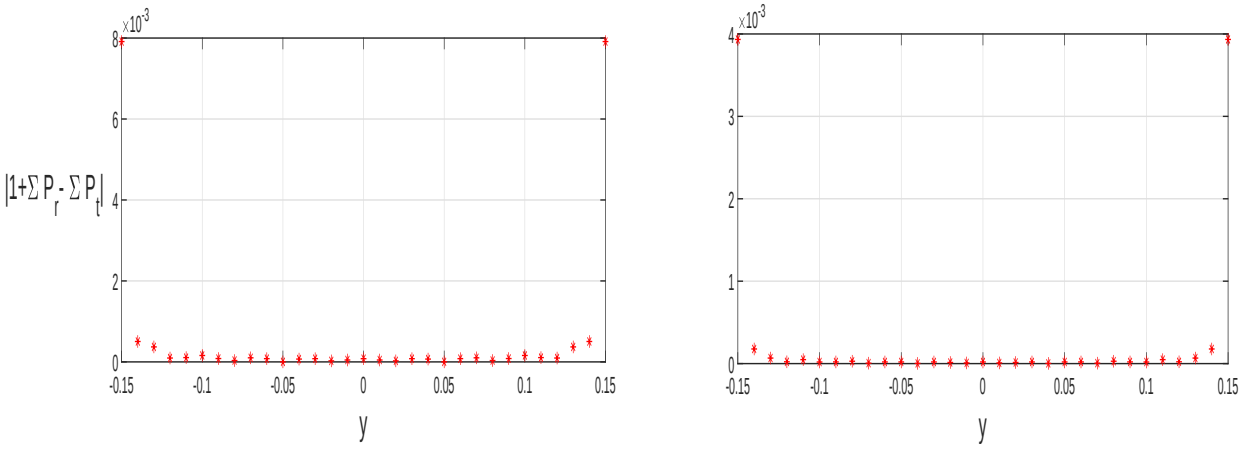

Figure 4.2: Pressure continuity at the interface ($x = 0$). Values presented are at the point $(0, 0)$ for $f = 500Hz$. The figures differ by 100 modes (left) and 200 modes (right) to illustrate how the pressure difference approaches zero as more modes are taken.

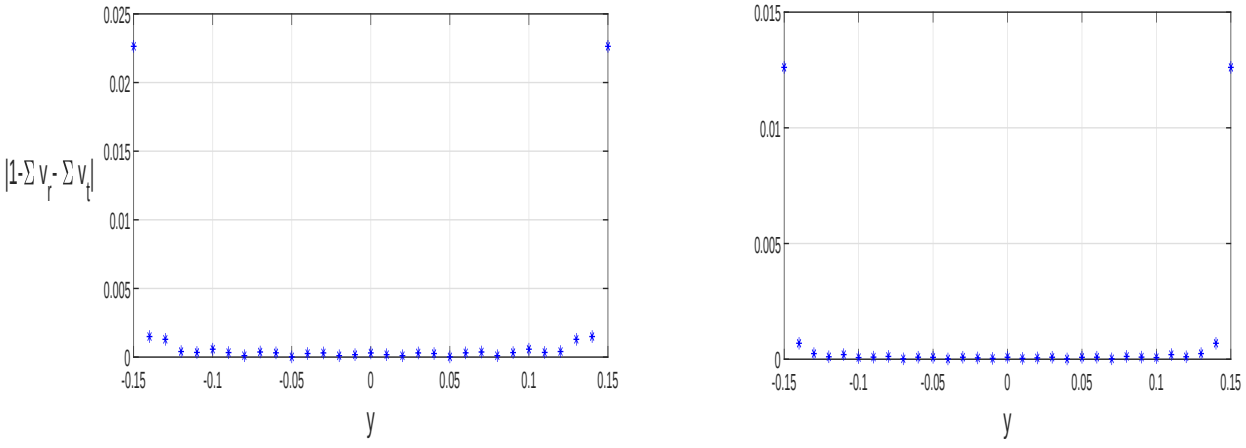

Figure 4.3: Velocity continuity at the interface ($x = 0$). Values presented are at the point $(0, 0)$ for $f = 500Hz$. The figures differ by 100 modes (left) and 200 modes (right) to illustrate how the velocity profile difference approaches zero as more modes are taken.

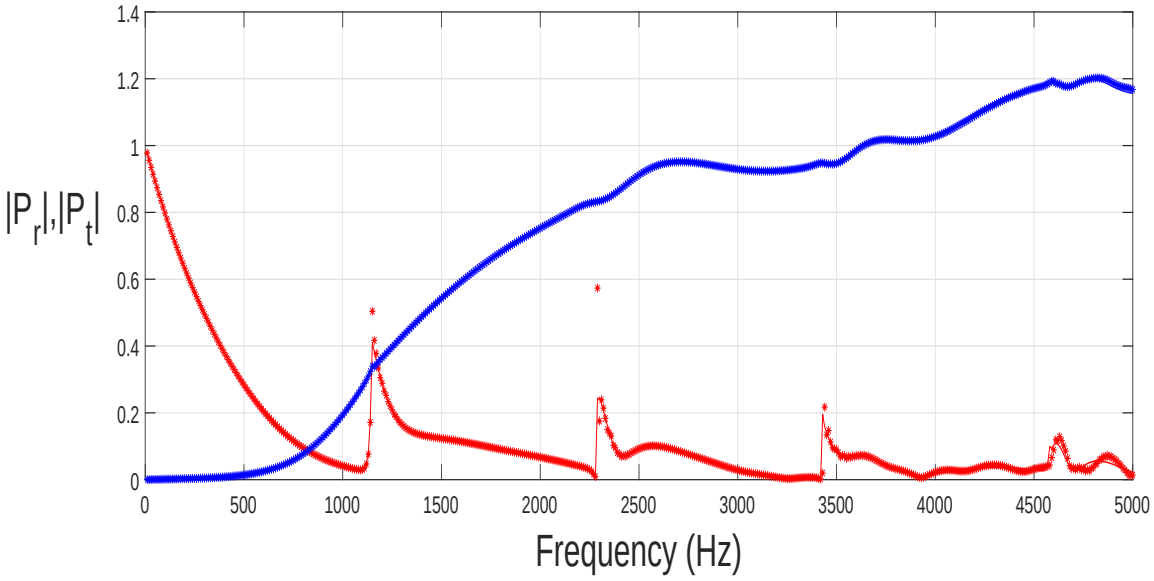

Figure 4.4: Matrix solution compared with a finite elements simulation (COMSOL) for a two-dimensional waveguide with an incident plane wave of unity incoming onto a acoustically hard/impedance discontinuity. Reflection is differentiated from transmission by color (red for reflection and blue for transmission) while matrix and FEM methods of solutions are differentiated by lines an "*"'s, respectively. Waveguide width is kept at a constant value of $h = 0.3$m. Both measurements are taken from 0.5m away from the interface on both sides and on the centerline.

In practice, it is advantageous to measure the energy loss in the presence of attenuation and damping caused by the impedance wall conditions. This is calculated by first introducing the following:

$$R_e = \frac{\int_{-h/2}^{h/2} |P_r|^2 dy}{\int_{-h/2}^{h/2} |P_{inc}|^2 dy}, \qquad T_e = \frac{\int_{-h/2}^{h/2} |P_t|^2 dy}{\int_{-h/2}^{h/2} |P_{inc}|^2 dy}. \tag{4.9}$$

R_e and T_e can be thought of the reflected and transmitted energies at a fixed x. With that said, we can now define what we will refer to as the absorption coefficient μ, a non-dimensional measure of energy loss

$$\mu = 1 - R_e - T_e. \tag{4.10}$$

It is important to note that R_e and T_e are not equal to the previously used reflection and transmission coefficients, R and T. Figure 4.5 depicts absorption coefficients for three different α values with varying real part and equal imaginary part. This is done in order to erase any stipulation that would be caused for changing the resistive portion of the impedance, i.e. the imaginary part of α. All are centered around a slight change in the first symmetric double root α (on the order of $O(10^{-4})$) with different perturbations from then on. The perturbation have been restricted to just changing $\Re\alpha$ and range from zero (red), $+0.3$ (blue) and -0.3 (green). For the majority of studied

frequencies, the case closest to the double root α experiences the highest absorption as expected, However, for some lower frequencies this is not the case. This can be attributed to higher back-pressure, and therefore more energy reflected back for that of the red case compared to the others. Also note the slight dip for all three occurring at about 1130 Hz. A direct link can be drawn to this and the cut-on frequency of the next mode which occurs at that particular frequency for a waveguide with acoustically rigid walls. Absorption curves of hard-perforated hybrid waveguides are illustrated in figures 4.6 and 4.7. Their performance regarding energy dissipation seems lackluster when juxtaposed with μ for a hard-EP impedance hybrid system.

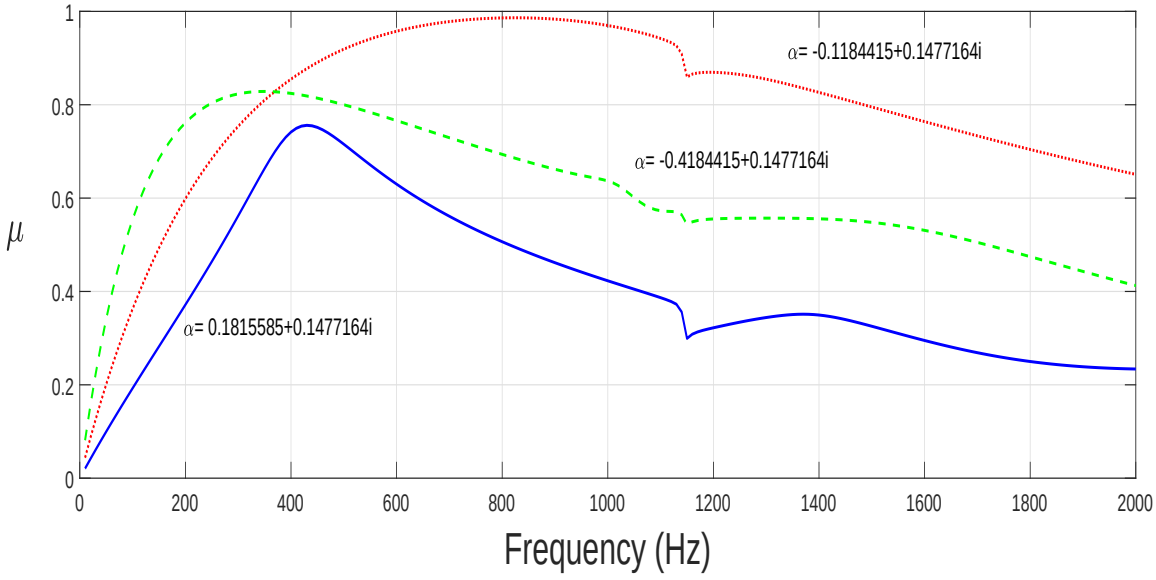

Figure 4.5: Three separate absorption coefficients measured at different α values with varying real part and constant imaginary part.

4.2 One discontinuity terminated by a rigid boundary

We seek out to set up the preliminary work required to verify our claims experimentally which requires an accurate model of the test methods being used. Consider the axisymmetric 3D waveguide discussed in section 2.3 containing an impedance discontinuity located at $x = 0$ and a rigid termination located at $x = a$ seen in figure 4.11. There are several variations of experimental procedures discussed in section 5.2 that incorporate a rigid wall at the end of the testing apparatus so for comparison purposes we include one in the model. The following pressures involved are defined as

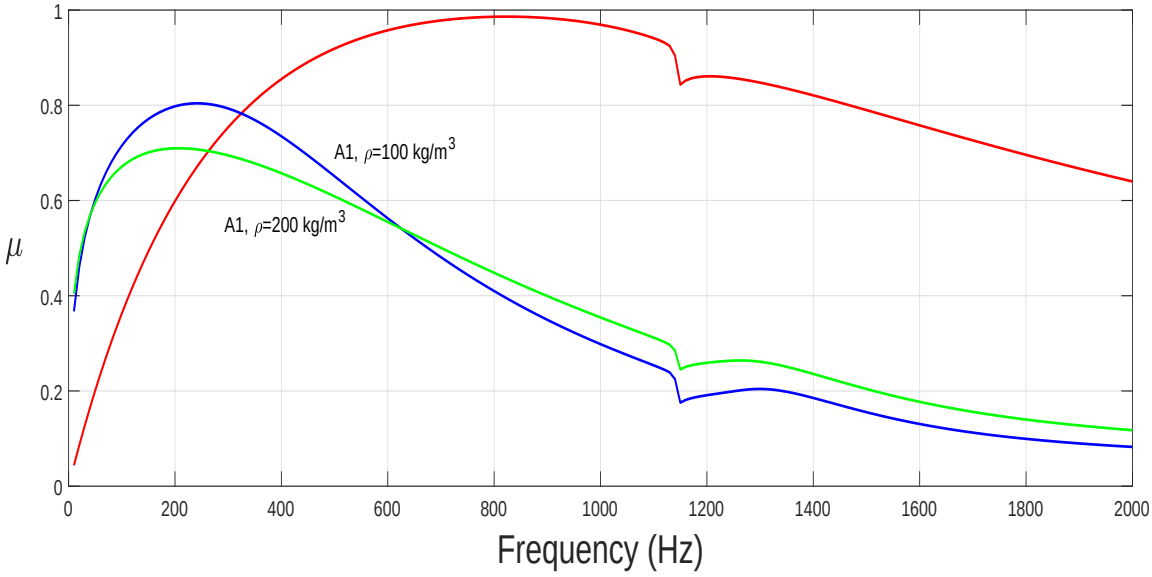

Figure 4.6: Three separate absorption coefficients measured at different α values. Red defines an α value around the first symmetric double root, while blue and green are the absorption coefficients for α's with regard to perforated plate impedances studied in the appendix. Specifically, blue is for plate A1 with a fibrous material lining of $\rho = 100kg/m^3$ and green is for plate A1 with a fibrous material lining of $\rho = 200kg/m^3$.

such,

$$P_{in} = \psi_{in}^{(L)}(y)e^{i\gamma_{in}kx}, \qquad P_{r1} = \sum_{m=1}^{\infty} R_m\psi_m^{(L)}(y)e^{-i\gamma_m kx},$$
$$P_{r2} = \sum_{n=1}^{\infty} R'_n\psi_n^{(M)}(y)e^{-i\theta_n kx}, \qquad P_{t1} = \sum_{n=1}^{\infty} T_n\psi_n^{(M)}(y)e^{i\theta_n kx}, \tag{4.11}$$
$$\text{where } \psi_n(r) = J_0(\frac{\beta_n r}{b}),\ \gamma_m = \sqrt{1-(\frac{\beta_m}{kb})^2},\ \theta_n = \sqrt{1-(\frac{\beta_n}{kb})^2}.$$

As explained in the previous section, "inc" establishes the incoming forward-traveling wave and $\phi_m^{(L)}(y)/\gamma_m$ ($\phi_n^{(R)}(y)/\theta_n$) is the eigenfunction/effective wave number pair present in the portion of the waveguide that is influenced by the wall impedance Z_A (Z_B). Once again we have pressure and velocity continuity at the interface separating the two wall impedances, however, we introduce a third condition to incorporate the effect of adding a rigid termination; the velocity at $x = a$ must

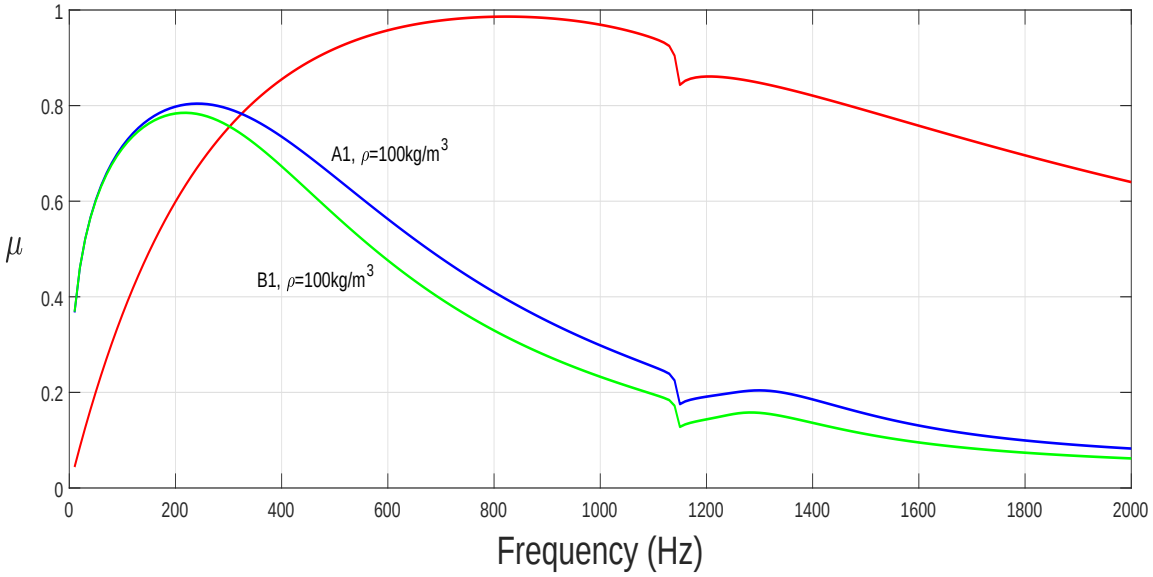

Figure 4.7: Three separate absorption coefficients measured at different α values. Red defines an α value around the first symmetric double root, while blue and green are the absorption coefficients for α's with regard to perforated plate impedances studied in the appendix. Specifically, blue is for plate A1 with a fibrous material lining of $\rho = 100kg/m^3$ and green is for plate B1 with a fibrous material lining of $\rho = 100kg/m^3$.

be zero. Both condition types take the form

$$
\begin{aligned}
&x = 0 : \text{Pressure-Velocity} \\
&-\sum_{m=1}^{\infty} R_m C_{nm} + (T_n + R'_n) b^2 H_n = A_n, \qquad \sum_{m=1}^{\infty} \gamma_m R_m C_{nm} + \theta_n (T_n - R'_n) b^2 H_n = \gamma_{inc} A_n, \\
&x = a : \text{Velocity} \\
&\theta_n (T_n e^{i\theta_n ka} - R'_n e^{-i\theta_n ka}) b^2 H_n = 0,
\end{aligned}
\tag{4.12}
$$

with orthogonality of the eigenfunctions used to create the integral coefficients

$$
C_{nm} = \int_0^b \phi_n^{(R)}(r)\phi_m^{(L)}(r) r dr, \qquad H_n = \int_0^b (\phi_n^{(R)}(r))^2 r dr, \qquad A_n = \int_0^b \phi_n^{(R)}(r)\phi_{in}^{(L)}(r) r dr. \tag{4.13}
$$

(4.13) can be simplified with the help of Bessel function identities to

$$
\begin{aligned}
C_{nm} &= \int_0^b \phi_n^{(R)}(r)\phi_m^{(L)}(r) r dr = \frac{\beta_m J_1(\beta_m) J_0(\beta_n) - \beta_n J_1(\beta_n) J_0(\beta_m)}{(\frac{\beta_m}{b})^2 - (\frac{\beta_n}{b})^2}, \\
An &= \int_0^b \phi_n^{(R)} r dr = \frac{b^2}{\beta_n} J_1(\beta_n) \text{ when } \phi_{in}^{(L)} = 1, \\
H_n &= \Big(J_0^2(\beta_n) + J_1^2(\beta_n) \Big)/2.
\end{aligned}
\tag{4.14}
$$

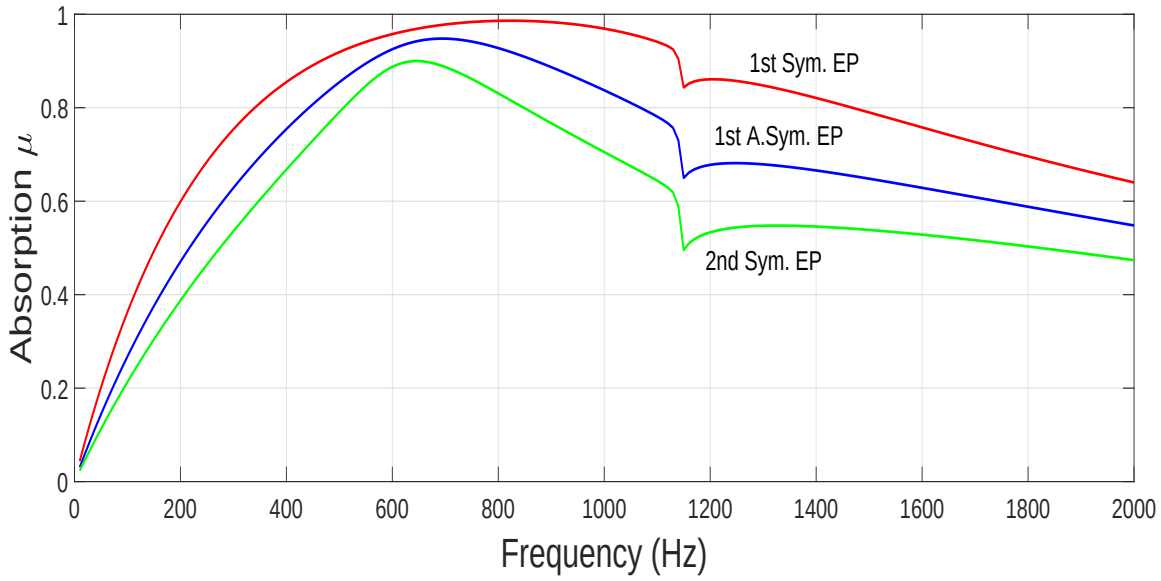

Figure 4.8: Three absorption curves for exceptional point cases where different modes are coalesced. Red defines an α value around the first symmetric double root, while blue and green is for an α value around the first asymmetric double root and second symmetric double root, respectively.

$\phi_{in}^{(L)} = 1$ is assuming plane wave incidence. Equation (4.12) has a matrix form that is advantageous for numerically determining the unknown reflection and transmission coefficients R_m, R'_n and T_n,

$$\begin{bmatrix} -C_{nm}^{NxM}, & b^2 H_n I^{NxN}, & b^2 H_n I^{NxN} \\ \gamma_m C_{nm}^{NxM}, & -b^2 \theta_n H_n I^{NxN}, & b^2 \theta_n H_n I^{NxN} \\ 0^{NxM}, & -b^2 \theta_n e^{-i\theta_n ka} H_n I^{NxN}, & b^2 \theta_n e^{i\theta_n ka} H_n I^{NxN} \end{bmatrix} \begin{pmatrix} R_M \\ R'_N \\ T_N \end{pmatrix} = \begin{pmatrix} A_N \\ A_N \\ 0^{Nx1} \end{pmatrix}. \tag{4.15}$$

Unfortunately, the matrix of (4.15) has the tendency to have a high degree of singularity with singularity increasing with matrix size (determined by how many modes are needed to accurately define the system). A way was discovered to combat this by revisiting the termination velocity condition at $x = a$:

$$\begin{aligned} &x = a : \text{Velocity} \\ &\theta_n (T_n e^{i\theta_n ka} - R'_n e^{-i\theta_n ka}) b^2 H_n = 0 \rightarrow R'_n = T_n e^{2i\theta_n ka}, \end{aligned} \tag{4.16}$$

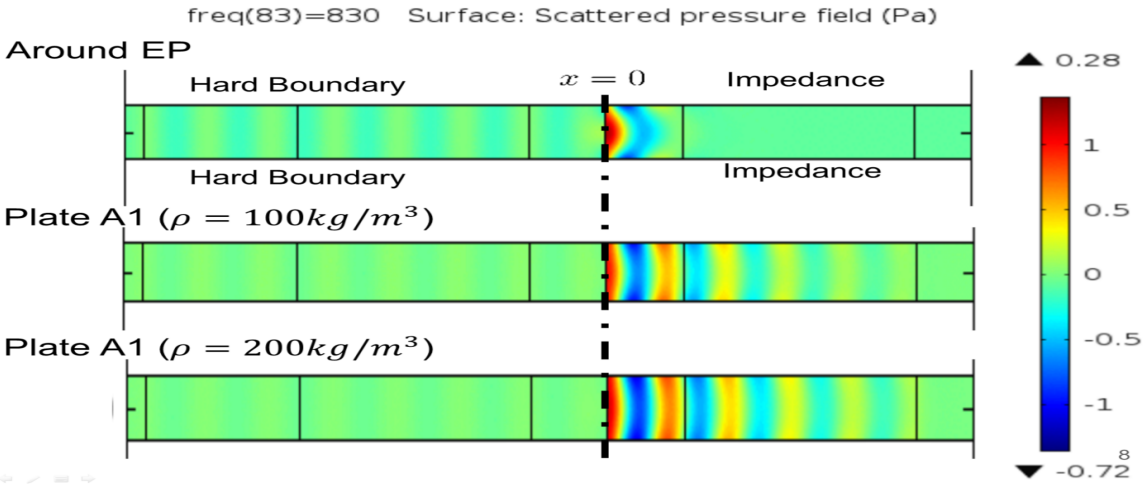

Figure 4.9: Simulation results of waveguide with impedance discontinuity at 830 Hz and h=0.3m using COMSOL. The wall impedance descriptions are as follows: Top: $x < 0$ hard and $x > 0$ around EP impedance, Middle: $x < 0$ hard and $x > 0$ perforated impedance with fibrous lining ($\rho = 100kg/m^3$), Bottom: $x < 0$ hard and $x > 0$ perforated impedance with fibrous lining ($\rho = 200kg/m^3$). Perforated impedance values measured through the use of equation (B.1) and tables 6.2-6.3.

redefining matrix (4.15) to

$$\begin{bmatrix} -C_{nm}^{NxM}, & b^2 H_n(1+e^{2i\theta_n ka})I^{NxN} \\ \gamma_m C_{nm}^{NxM}, & b^2\theta_n H_n(1-e^{2i\theta_n ka})I^{NxN} \end{bmatrix} \begin{pmatrix} R_M \\ T_N \end{pmatrix} = \begin{pmatrix} A_N \\ A_N \end{pmatrix} \tag{4.17}$$

$$R'_n = T_n e^{2i\theta_n ka}.$$

(4.16) does not exhibit the singularity problem of the previous matrix and we can continue with the analysis. By solving an example with our model and comparing it to that of a FEM simulation we will be able to test the legitimacy of the model in addition to erasing any questions regarding it's accuracy. The problem we'll consider will consists of the axisymmetric waveguide terminated by a rigid plate which will start with acoustically hard walls ($|Z_A| = \infty$) and transition to an EP wall impedance ($_B = Z_{ep}$) via the discontinuity. Z_{ep} is calculated via equation (3.23) where we will be using the first EP mode that satisfies (3.22), $\beta_q = 2.9804 - 1.2796i$. When the walls are hard the eigenvalue equation of (2.31) become $J_1(\beta_m) = 0$. The first ten modes for both waveguide partitions are illustrated in figure 4.12. Note the mode coalescence in 4.12(a). Because of the rigid termination at the end, transmission energy is not able to propagate away from the interface and will only be

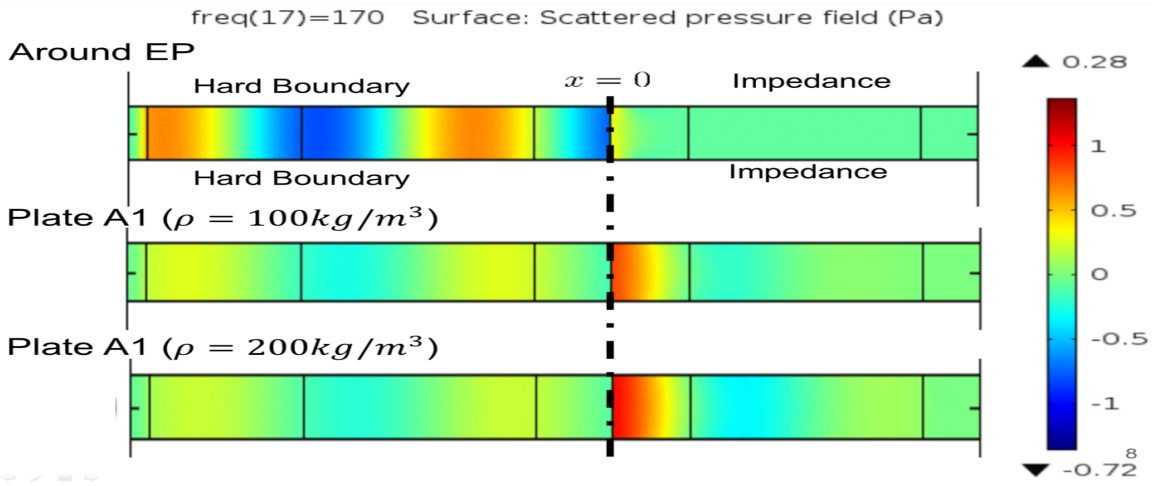

Figure 4.10: Simulation results of waveguide with impedance discontinuity at 830 Hz and h=0.3m using COMSOL. The wall impedance descriptions are as follows: Top: $x < 0$ hard and $x > 0$ around EP impedance, Middle: $x < 0$ hard and $x > 0$ perforated impedance with fibrous lining ($\rho = 100kg/m^3$), Bottom: $x < 0$ hard and $x > 0$ perforated impedance with fibrous lining ($\rho = 200kg/m^3$). Perforated impedance values measured through the use of equation (B.1) and tables 6.2-6.3.

reflect back towards it. It is because of this fact that we redefine the absorption coefficient as

$$\mu = 1 - R_e, \text{ where } R_e = \frac{\int_0^b |P_{R1}|^2 r dr}{\int_0^b |P_{inc}|^2 r dr}. \tag{4.18}$$

This is analogous to the absorption performance of porous material backed by a rigid plate. The energy being dissipated by the porous sample can be determined solely by the ratio of reflected energy at its surface to that of incident energy without directly considering the wave behavior inside of it. This is typically done experimentally with the use of two microphones measuring inside the hard portion of the tube, $x < 0$, with the use of signal processing techniques to differentiate the incoming and reflected pressure fields (a common test method seen in 5.2). Utilization of (4.11) with (4.17) completely defines the system and their results are presented in figure 4.13. Results are also compared side-by-side to the solution generated by a FEM simulation with COMSOL. Accuracy is shown to be satisfactory with agreement increasing with number of modes used for the model.

Now with an established legitimacy of the matrix method (4.17), absorption curves for any uniform wall impedances Z_A and Z_B are possible to obtain. Another test is done where Z_B is switched for a perforated plate impedance found in appendix B. to compare with the EP wall impedance. The outcome is depicted in figure 4.14 and inspection clearly shows that EPs possess a large amount of potential with this regard keeping in mind that perforated plates are a common tactic used in passive energy dissipation in waveguides.

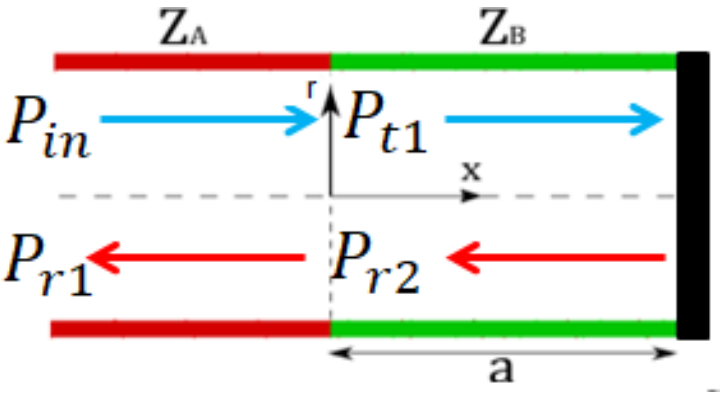

Figure 4.11: Depiction of waveguide model for various test methods. Includes impedance discontinuity at $x = 0$ and rigid plate termination at $x = a$. Respective incoming, reflected, and transmitted pressures are shown.

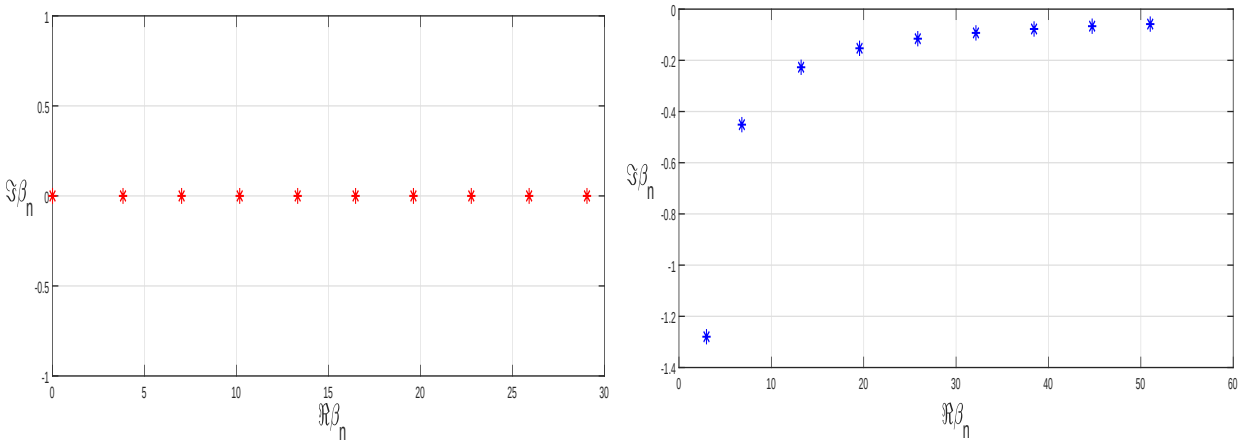

Figure 4.12: First ten modes for 3D axisymmetric waveguide with hard and EP impedance walls at $1000Hz$ and $b = 0.5$".

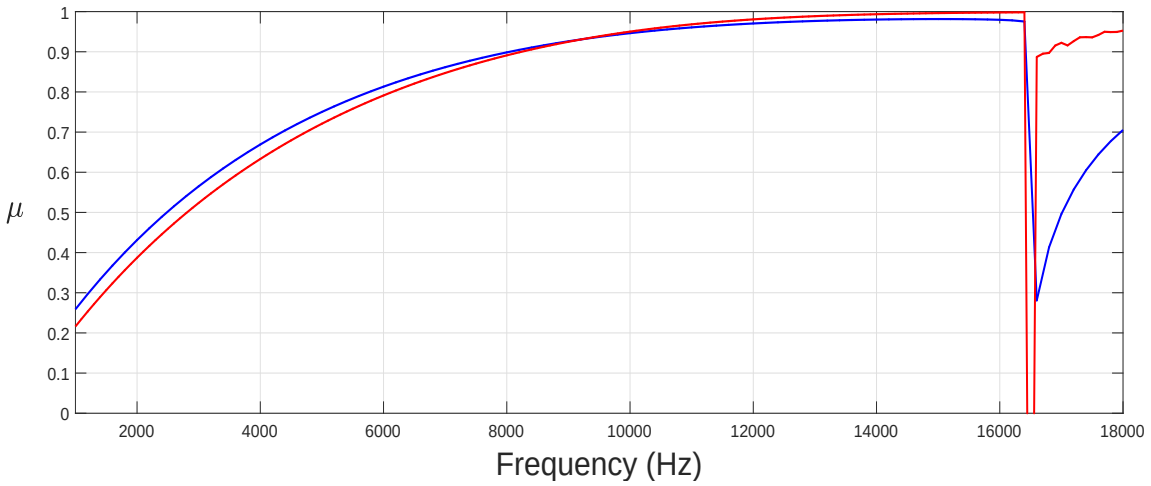

Figure 4.13: Absorption curves obtained via matrix model (blue) vs. COMSOL FEM simulation (red). Sudden drop linked to cut-on of second mode for acoustically hard walls.

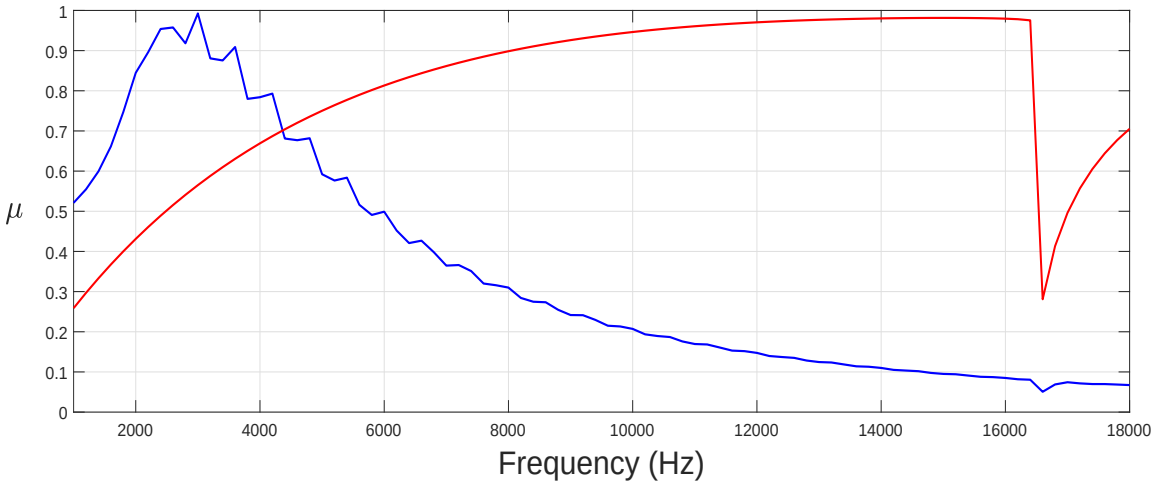

Figure 4.14: Absorption curves for $|Z_A| = \infty$ and $Z_B = Z_{ep}$ (red) verse $|Z_A| = \infty$ and $Z_B = Z_{perforated}$ (blue).

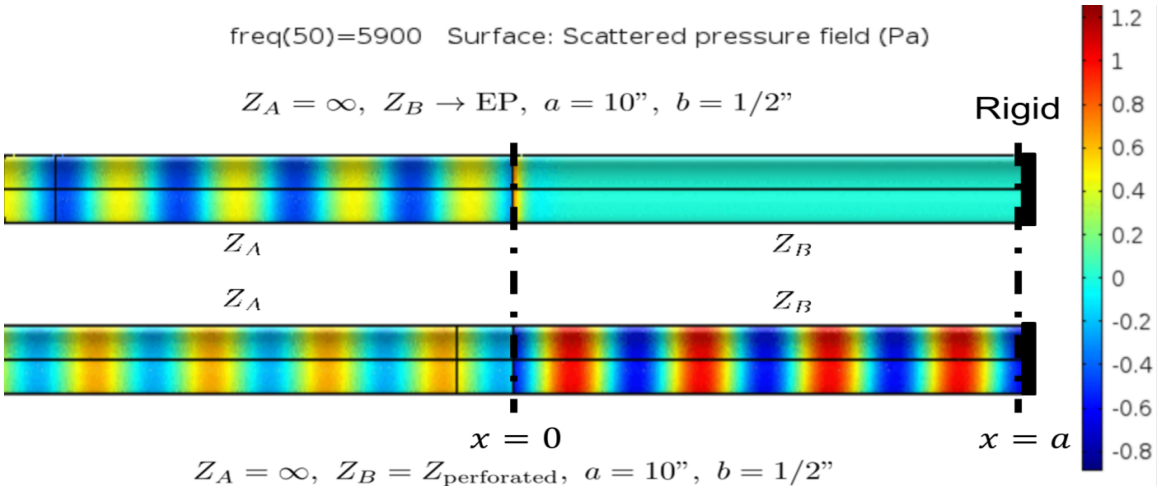

Figure 4.15: Simulation results of waveguide with impedance discontinuity at 5900 Hz and b=0.5in using COMSOL. The wall impedance descriptions are as follows: Top: $x < 0$ hard and $x > 0$ around EP impedance, Bottom: $x < 0$ hard and $x > 0$ perforated impedance with fibrous lining ($\rho = 100kg/m^3$). Perforated impedance values measured through the use of equation (B.1) and tables 6.2-6.3.

Chapter 5
EP feasibility

This chapter discloses the next steps in the ongoing search for physically realizable double roots. We start with a deeper look into a general impedance to try and find physical constraints. It will serve as a starting point into the investigation of realistic EPs where we will answer the question can a simple system exhibit double roots, is one of higher complexity needed, or are they not within the realm of possibility. What follows is the introduction to a test method which may be used to justify theorized EP impedances through experimental validation if they are found to be possible.

5.1 Physical constraints

EP impedance walls have demonstrated to be an above average tool in energy absorption for uniform waveguides. While the above chapter suggests better performance for a wide range of frequencies, the obvious next question becomes how is this achieved realistically? Perforates have served as our go to real-world comparison due to how common they are for this purpose, however, their impedance models (while arguably slightly different from Lee's [9]) can never exhibit EP behavior. This claim is evident when inspecting the impedance of perforated plates (B.1) to that of an impedance generating EPs for the lowest two symmetric modes

$$\begin{aligned} Z_{ep} &= \omega h\rho(0.1478 + i0.1184) \text{ (2-D planar WG)}, \\ Z_{ep} &= \omega b\rho(0.2833 + i0.1216) \text{ (axisymmetric cylindrical WG)}. \end{aligned} \tag{5.1}$$

The main difference being the positive linear frequency dependence of both the resistive and reactive portion of Z_{ep}. That is, to acquire a wall impedance equal to that of equation (5.1) for their respective cases would have the first two symmetric modes coalescing for every frequency. In order to continue further with the investigation of feasibility for exceptional points, it is first beneficial to consider any physical constraints regarding impedance values in general. As stated previously, an $e^{-i\omega t}$ dependence is omitted but understood leading to the derivation of equation (2.7) stated again here:

$$Z = \zeta - i\omega M + \frac{iK}{\omega} \tag{5.2}$$

where M is an inertial component, K is a bulk modulus component, and ζ is a damping factor. A plethora of different impedance models like that of Helmholtz resonators, membranes, porous media, etc. have impedances that take on this form. We start by performing a lumped parameter study of various passive and lossless acoustic networks (analogous to electrical networks) as seen in [15]. To clarify, think of a lumped acoustic network as a multiple degree of freedom mass-spring systems interconnected. Each equation of motion will consist of individual terms which correlate to specific masses and cross terms which physically represent the mutual dependence of one mass on the other, varying only by how they are connected. In equation form, this appears as the system

$$\begin{cases} z_{11}u_1 + z_{12}u_2 + \ldots + z_{1n}u_n = p_1 \\ z_{21}u_1 + z_{22}u_2 + \ldots + z_{2n}u_n = 0 \\ \ldots\ldots\ldots\ldots\ldots\ldots\ldots\ldots \\ z_{n1}u_1 + z_{n2}u_2 + \ldots + z_{nn}u_n = 0 \end{cases} \tag{5.3}$$

where p_1 is the driving pressure, u's are the network particle velocities, and

$$z_{rs} = z_{sr} = \frac{iK_{rs}}{\omega}\Big(1 - \frac{\omega^2}{\omega'^2_{rs}}\Big),\ \omega'_{rs} = \sqrt{\frac{K_{rs}}{M_{rs}}} \tag{5.4}$$

are the mesh (r=s) or mutual impedances (r $\neq$ s). More favorably, it is possible to write equation (5.3) into a fairly simple matrix form

$$\mathbf{z}\overrightarrow{u} = \overrightarrow{p}$$

$$\mathbf{z} = \begin{bmatrix} z_{11} & z_{12} & z_{13} & \cdots & z_{1n} \\ z_{21} & z_{22} & z_{23} & \cdots & z_{2n} \\ \vdots & \ddots & & & \vdots \\ \vdots & & \ddots & & \vdots \\ \vdots & & & \ddots & \vdots \\ z_{n1} & z_{n2} & z_{n3} & \cdots & z_{nn} \end{bmatrix},\ \overrightarrow{u} = \begin{pmatrix} u_1 \\ \vdots \\ u_n \end{pmatrix},\ \overrightarrow{p} = \begin{pmatrix} p_1 \\ 0 \\ 0 \\ \vdots \\ 0 \end{pmatrix}. \tag{5.5}$$

Solving (5.3) for velocities yields

$$\overrightarrow{u} = \mathbf{z}^{-1}\overrightarrow{p} = \frac{\mathbf{A}^T\overrightarrow{p}}{D} = \frac{\mathbf{A}\overrightarrow{p}}{D} \tag{5.6}$$

where $\mathbf{A}$ is the matrix of cofactors of $\mathbf{z}$ and D is the determinant of $\mathbf{z}$. Note that $\mathbf{A} = \mathbf{A}^T$ due to the symmetrical nature of $\mathbf{z}$. simplifying (5.6) further leads to

$$u_r = \frac{A_{1r}p_1}{D} \tag{5.7}$$

due to the fact that the only nonzero element in $\overrightarrow{p}$ is the first element. Therefore the driving-point impedance, or input impedance, of the acoustic network is

$$Z_{11} = \frac{p_1}{u_1} = \frac{D}{A_{11}}. \tag{5.8}$$

The following can be drawn from equation (5.7): the resonances of the acoustic network are related to the zeros of D and the antiresonances relate to the zeros of A_{11}. An impedance requires a positive linear frequency response or regime in order to meet the conditions for exceptional points with an $e^{-i\omega t}$ dependence. With that being said, it is imperative to look at the slope of the driving-point impedance of any general acoustic network to gauge it's feasibility. Differentiating (5.8) gives

$$\frac{\partial Z_{11}}{\partial(i\omega)} = -\frac{p_1}{u_1^2}\frac{\partial u_1}{\partial(i\omega)}, \text{ where } \frac{\partial u_1}{\partial(i\omega)} = \sum_{s=1}^{n} G_s A_{1s} \text{ and } G_s = \frac{1}{D}\sum_{r=1}^{n}\Big(M_{rs} + \frac{K_{rs}}{\omega^2}\Big)u_r. \tag{5.9}$$

Note that $\frac{\partial u_1}{\partial(i\omega)}$ was found via differentiating (5.5) by $i\omega$ and variable isolation. Substitution of (5.7) for the A_{1s}'s yields

$$\frac{\partial u_1}{\partial(i\omega)} = \frac{1}{p_1}\Big(\sum_{r,s=1}^{n}\frac{u_r u_s K_{rs}}{\omega^2} + \sum_{r,s=1}^{n} u_r u_s M_{rs}\Big). \tag{5.10}$$

Further inspection of the two terms associated with (5.10) shows that they are in fact the total potential and kinetic energies, respectively, for an n degree of freedom system which is time harmonic i.e.

$$V = -\frac{1}{2}\sum_{r,s=1}^{n}\frac{u_r u_s K_{rs}}{\omega^2},\ T = -\frac{1}{2}\sum_{r,s=1}^{n} u_r u_s M_{rs}. \tag{5.11}$$

Both terms can be physically interpreted as being always positive. (5.10) can be written as

$$\frac{\partial u_1}{\partial(i\omega)} = \frac{2}{p_1}\Big(V + T\Big) \tag{5.12}$$

redefining (5.9) to

$$\frac{\partial Z_{11}}{\partial(i\omega)} = \frac{2}{u_1^2}\Big(V + T\Big). \tag{5.13}$$

For a real driving pressure p_1, u_1 will be purely imaginary concluding that the driving-point impedance will always be decreasing with increasing frequency, also referred to as Foster's theorem for an acoustic system. For all the cases previously studied, waveguides varying in wall impedance with and without discontinuities act as limiting cases to the lumped parameter study. In more detail, those cases behave as distributed systems which can be modeled as a large number of infinitesimal constituents, each having the nature of a lumped element as stated by Maa [15]. The observation

implies that Foster's theorem will apply to them as well. As for final remarks, in order to have the necessary linearly increasing frequency dependence necessary for exceptional points, either a negative bulk modulus, negative mass density, or a combination of the two is required.

5.2 Test methods

The purpose of this section serves to give detail on a test method used in order to determine the acoustic response of, for the most part, any sample. The general purpose for this technique is to classify the acoustic response of porous media, however, it can be useful in determining physically realizable EP behavior. Code used and preliminary results are given in addition to possible sources of error.

5.2.1 Two-mic transfer function method

The general layout for the two-microphone method is shown in figure 5.1 which highlights the necessary equipment. Specifically, the overall process requires two microphones (hence the name), a speaker, a rigid pipe, a rigid termination, a function generator capable of frequency sweeps and signal processing equipment i.e. a data acquisition board (DAQ). The microphones do not need to be moved unless calibration is necessary. Tests using the two-mic method have to be operated within a certain frequency range. This is to account for accuracy of the equipment used in addition to a plane wave assumption. In equation form this is

$$s > \frac{0.01c}{f_l}, \qquad \frac{c}{2s} << f_u < \begin{cases} \dfrac{0.586c}{d} \text{ or} \\ \dfrac{0.4c}{s}, \end{cases} \tag{5.14}$$

where s is microphone spacing, c is the fluid medium sound speed, d is the diameter of the tube, f_l is the lower frequency limit, and f_u is the upper frequency limit. Note that f_u is dictated by the smaller of the two bracketed terms. A plane wave frequency sweep is generated by the speaker/function generator that travels down the tube until it meets the sample where energy is reflected and transmitted. The energy that is transmitted is assumed to be completely reflected back at the rigid termination as depicted and modeled in section 4.2. Using a signal processing parameter known as a transfer function, H_{12} (also commonly referred to as a frequency response function), the data received from the microphones is able to be decomposed into incident and reflected pressure fields. H_{12} can be calculated via the auto and cross spectrum which is equivocally the ratio of the Fourier transforms of the measured pressure seen here:

$$H_{12} = \frac{G_{12}}{G_{11}} = \frac{S_1 S_1^*}{S_1 S_2^*} \text{ where } S_n = \mathfrak{F}(p_n),\ n = \text{mic number}. \tag{5.15}$$

Note "*" signifies complex conjugates. The reflection coefficient is now defined as

$$R = \frac{H_{12} - e^{-iks}}{e^{iks} - H_{12}} e^{2ikx_1}, \tag{5.16}$$

where x_1 is the distance between the start of the sample to the furthest microphone. With the reflected fields in hand, one may calculate the absorption coefficient and the surface impedance with the following relations:

$$\mu = 1 - |R|^2, \ Z_s = \rho c \frac{1+R}{1-R}, \ \rho = \text{fluid medium density}. \tag{5.17}$$

μ in (5.17) is a limiting case of (4.18) when there is only one plane wave mode present. More detail regarding this method is given in [16]. A more complicated test, like that discussed in [18], is needed for the direct measurement of characteristic impedance and complex wave number.

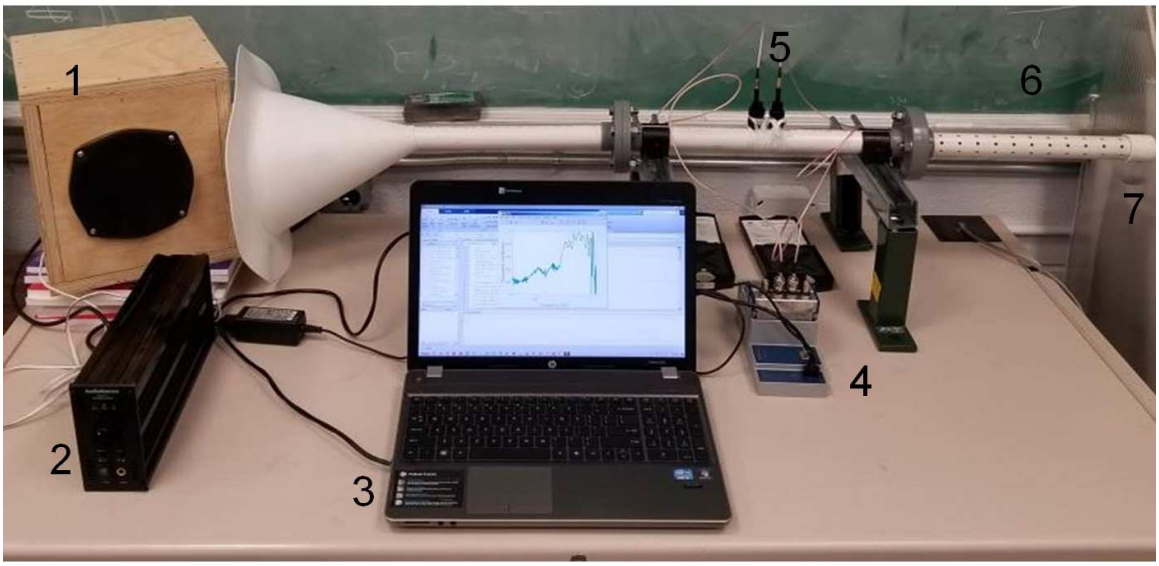

Figure 5.1: Setup of custom made impedance tube. Figure labeling goes as follows: 1) speaker 2) amplifier 3) computer running MATLAB 4) DAQ board 5) microphones flush with inside of tube 6) sample 7) rigid end cap.

5.3 Implementation and results

An impedance tube was designed and constructed around the criteria stated in [16]. The upstream tubing and perforated cylindrical sample were made out of 1 inch (.0254 m) in diameter schedule-40 PVC and were connected via PVC flanges. A 6 inch full range driver speaker is used and powered by a 5.1A AudioSource mono-block amplifier supplying 100 Watts at 4 Ω in addition to being housed by a wooden box to minimize any back reverberation. A PVC cone 10 inch (.254 m) in length

connects the speaker to the upstream tube while also serving as a sound funnel. When a test is initiated, a function generator phone application generates a frequency sweep played by the speaker. The pressure field in the upstream tube during the duration of the test is acquired through the use of two Brüel & Kjaer multi-field microphones spaced $1\frac{1}{8}$ inch apart connected to a NI 9234 module inside a NI cDAQ 9284 chassis. Due to the microphone spacing and tube diameter the frequency range measurable is approximately $200 < f < 4500$ Hz to comply with the constraints explained in equation (5.14). All pre and post-processing is done with a laptop running MATLAB. It was also found that the MATLAB operation "tfestimate" proved to result in accurate transfer functions in a time efficient manner.

Preliminary results of experiments run with a perforated PVC cylinder sample with dimensions length: 12", hole diameter: 0.919", hole spacing: 1", and porosity: 8.1% is presented below. Note that the absorption coefficient in figure 5.2 was normalized with respect to the absorption curve of tests run with an empty tube to account for any unaccountable absorption. Inspection of figure 5.2

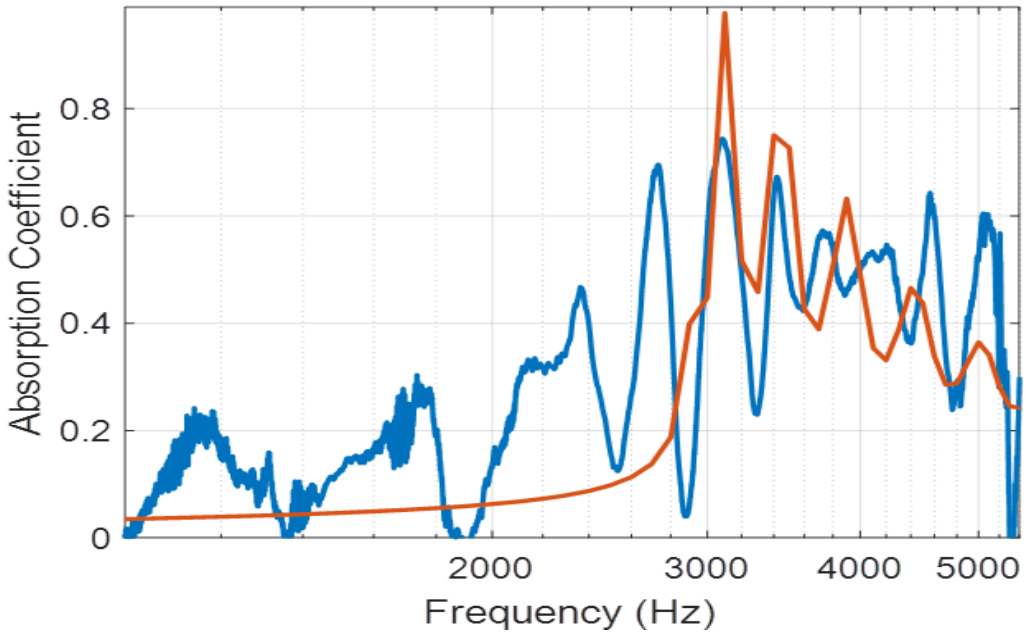

Figure 5.2: Absorption curves for a perforated sample made experimentally (blue) and computationally through COMSOL (red).

tells us that the overall shapes of the curves are in agreement, however the experimental setup is exhibiting higher than expected absorption values especially for low frequencies. This effect may be attributed to the fact that the cone was not completely flush to the speaker housing which might have led to air leakage causing the absorption to read higher than normal. One might look

into adopting a smaller speaker approach that way all airtight PVC and PVC connectors may be used to remedy this problem. Additionally, it has been noted by [17] that custom-made tubes with smaller diameters tend to read higher absorption values compared to that of industrial-grade prebuilt impedance tube especially when empty. A physical argument can be made that if a tube is not properly clean or contains rough surfaces, the plane wave assumptions can become less valid and a viscous boundary layer originating at the inner surface of the tube can lend itself to higher than average energy dissipation. Matlab code for the two-mic transfer function method is provided in the appendix.

Chapter 6
Conclusion

A general sense of the effects EPs have on waveguide solutions is developed through analytical, numerical and computational studies. Chapter 2 discusses waveguide modeling techniques for a two and three dimensional case in order to create a foundation in which to build off of. Properties like that of phase speeds, group speeds, and modal dependencies are explored for a 2D waveguide with equal impedance on both walls. Perturbation method is applied to the zeroth mode to explain its associated group speed value through an analytical approach.

EP conditions for both cases are derived by considering non-separable solutions to the Helmholtz equation and mode coalescence is demonstrated in chapter 3. First variations of conditions are reworked in order to obtain explicit expressions for EP wall impedance that depend solely on what mode one wants to coalesce. From these conditions stem simplified limiting cases and constraints on EP impedance values made to comply with passive impedance conditions. The traditional Green's function solution is shown to fail at modes that satisfy the EP conditions, but is fully defined around that value.

A matrix model is developed in chapter 4 for problems containing impedance discontinuities and side-by-side comparisons are done of the model with FEM simulations via COMSOL. Results show great agreement and the model is then utilized to generate absorption curves for waveguides with portions of the wall having EP impedance values. Inspection of the resulting curves conclude that EPs are a promising phenomenon regarding broadband absorption for both the two and three dimensional cases and preform better than perforated walls with and without fibrous linings. Snapshots of COMSOL simulations are also supplied for visual representation of the resulting pressure fields.

Feasibility of EPs is addressed in chapter 5; it is rationalized that the only way to obtain EP behavior is through negative parameters like that of mass density. For the sake of experimentally creating the theorized absorption curves of EP walled waveguides, a common impedance tube experiment is given with preliminary results and sources of error. Finding an analytic impedance model that exhibits the required double root impedance values discussed in chapter 5 is left for future work.

Appendix

A. Roots for a symmetric waveguide

Let $\beta_n = p - iq$, where we are looking for roots with $p \geq 0$, $q \geq 0$. The real and imaginary parts of Eq. $(3.10)_1$ become

$$\sin p \cosh q = \mp p, \tag{A.1a}$$

$$\cos p \sinh q = \mp q. \tag{A.1b}$$

The identities $\cos^2 p + \sin^2 p = 1$ and $\cosh^2 q - \sinh^2 q = 1$ allow us to write p in terms of q, and *vice versa*: $p = \cosh q\sqrt{1-(q/\sinh q)^2}$, $q = \mp\cos p\sqrt{(p/\sin p)^2 - 1}$. Using the first of these with (A.1b) gives

$$\sqrt{1-(q/\sinh q)^2}\,\cosh q = \cos^{-1}\left(\mp q/\sinh q\right) + 2m\pi \tag{A.2}$$

where m is an integer.

Equations (A.1) imply that the modally symmetric (antisymmetric) roots correspond to $\sin p = \cos p = -1(+1)$, respectively. Using this and (A.2) implies that the n^{th} symmetric and antisymmetric roots correspond to the $-$ and $+$ signs, respectively, where

$$p = \sqrt{1-(q/\sinh q)^2}\,\cosh q, \tag{A.3a}$$

$$\sqrt{1-(q/\sinh q)^2}\,\cosh q = \mp\frac{\pi}{2} - \frac{\pi}{2} + 2n\pi + \cos^{-1}\left(q/\sinh q\right) \tag{A.3b}$$

and the principal branch of $\cos^{-1}$ is used, i.e. from zero to $\pi/2$. Equation (A.3b) can be solved using the initial estimate $q \approx \cosh^{-1}(2n\pi \mp \frac{\pi}{2})$, and p then follows from (A.3a). In particular, for large values of n,

$$\beta_n \approx 2n\pi \mp \frac{\pi}{2} - i\ln 2\big(2n\pi \mp \frac{\pi}{2}\big). \tag{A.4}$$

B. Impedance models

B..1 Perforated plates

As a primary focus we consider the "straight-through" muffler, a cylindrical waveguide with perforated walls and absorbing material (such as fibrous foam) on the other side. Models for perforated panels as acoustic silencers have been studied exhaustively (with no pun intended), e.g. recent survey can be found in [8, 9, 10, 11]. Despite the successful application of acoustic principles in the development of this technology, there has been no overlap with the concepts first proposed by

Cremer. Our purpose is to fill this gap and provide a sound (again, NPI) basis for optimal damping in waveguides.

In models of perforated side walls the resistive component of the effective impedance arises from the air viscosity. This resistivity can be augmented by the addition of an absorbing fibrous material. The main contribution to the reactive part of the impedance arises from the geometry of the perforation (circular or slit like) to account for the inertial behavior of the column of air inside and around the perforate in addition to the end corrections that compensate for interactions between perforations. End corrections are typically perforation geometry and fluid medium dependent. Porosity, or the degree of perforation, will affect both the resistive and reactive component of the impedance. The equation form of the nondimensional impedance for a perforated plate with or without fibrous material proposed by Lee [9] looks like

$$\frac{Z_p}{Z_0} = \frac{R - ik(t_w + \delta d_h)}{\eta}, \tag{B.1}$$

where R is the dimensionless resistance, t_w is the wall thickness, d_h is the hole diameter, δ is the end correction, and η is the porosity. an $e^{-i\omega t}$ is omitted but understood. η will be defined as the ratio between the individual perforation and waveguide areas in conjunction with a proportionality to the number of perforations, i.e.

$$\eta = \frac{n_h A_h}{A_1}. \tag{B.2}$$

It is important to note that the resistive component of the impedance in equation (B.1) is assumed to be frequency independent, a fair assumption experimentally supported by [9]-[12]. Tables were provided of experimentally determined R and δ in Lee [9],

Plate	t_w (cm)	d_h (cm)
A	0.08	0.249
B	0.16	0.249
C	0.08	0.498

Table 6.1: Plate thickness and hole diameters

Plate	No fibrous	$\rho = 100\frac{kg}{m^3}$	$\rho = 200\frac{kg}{m^3}$
A1	0.007624	0.03054	0.04935
A2	0.005101	0.02996	0.04575
A3	0.004437	0.02298	0.03610
A4	0.004500	0.02716	0.04447
B1	0.008429	0.03133	0.05770
B2	0.006074	0.02793	0.04900
B3	0.005744	0.02444	0.04142
B4	0.005539	0.02657	0.05076
C2	0.005318	0.04728	0.09015
C3	0.005013	0.04598	0.09308
C4	0.004395	0.03973	0.07604

Table 6.2: Resistance R for different test samples. Let 1-4 correspond to a porosity of 2.1%, 8.4%, 13.6%, and 25.2% respectively.

Plate	No fibrous	$\rho = 100\frac{kg}{m^3}$	$\rho = 200\frac{kg}{m^3}$
A1	0.5350	0.6989	0.7769
A2	0.4409	0.6471	0.7412
A3	0.2506	0.4576	0.4999
A4	0.1286	0.4717	0.4590
B1	0.5179	0.6514	0.7663
B2	0.4224	0.6026	0.6758
B3	0.2666	0.4661	0.5048
B4	0.1066	0.3951	0.3980
C2	0.4707	0.6206	0.7167
C3	0.4473	0.6269	0.7142
C4	0.2471	0.4504	0.4926

Table 6.3: End Corrections δ for different test samples. Let 1-4 correspond to a porosity of 2.1%, 8.4%, 13.6%, and 25.2% respectively.

C. MATLAB code

```
clear all
close all
%% Code setup
duration=10;
x=.028575; %mic spacing 1 1/8"
x1=0.26035; %farthest mic to beginning of sample est. 10.5"
c=343;
fs = 51200; % sampling rate

%% Hardware setup
% Discover Devices that Support Microphones
devices = daq.getDevices();
deviceInfo = devices(1)
% Create Session and Add Microphone Channel
s = daq.createSession('ni');
s.addAnalogInputChannel('cDAQ9184-1C4D691Mod1', 1,'Microphone');
s.addAnalogInputChannel('cDAQ9184-1C4D691Mod1', 2,'Microphone');
% Set Sensor Properties
s.Channels(1).Sensitivity = 0.0547;
s.Channels(2).Sensitivity = 0.0648;
s.Channels
% Configure And Start Acquisition
s.DurationInSeconds = duration ;
s.Rate = fs;
disp('wait')
pause(2);
disp('now')
[data, time] = s.startForeground();
```

1.png

Figure 6.1: Two-mic transfer function MATLAB code part 1.

```
% Save Data
save('example.mat','data','time')

%get data
ptch1=data(:,1);
ptch2=data(:,2);
t=time(:,1);
%Transfer function
[H12,freq]=tfestimate(data(:,1),data(:,2),[],[],[],51200);


%wavenumber
k = (2*pi*freq)/c;
%Reflection coefficient
R = (H12-exp(-1i.*k.*x))./(exp(1i.*k.*x) - H12) .*exp(2.*1i.*k.*x1);

%absorption coefficient
absorption = 1 - abs(R).^2;

%Surface impedance
Z=1.2*c*(1+R)./(1-R);

%plot pressure channel 1 and 2
figure(1)
plot(t,ptch1,'LineWidth',2);
xlabel('time (s)','FontSize',16);
ylabel('Pressure channel 1','FontSize',16);
set(gca,'FontSize',14);
```

2.png

Figure 6.2: Two-mic transfer function MATLAB code part 2.

```
grid on

figure(3)

freq_low_limit=500;
freq_high_limit=6000;

%plot transfer function
plot(freq,abs(H12),'LineWidth',2);
xlim([freq_low_limit freq_high_limit]);
ylim([-10^2 10^2]);
grid on;
xlabel('Frequency (Hz)','FontSize',16);
ylabel('Transfer Function H_{12}','FontSize',16);
set(gca,'FontSize',14);
saveas(gcf,'tf.fig');
print('tf', '-dpng', '-r600'); %Save as PNG with 600 DPI

% Coefficients
figure(4)
plot(freq,absorption, 'LineWidth',2);
xlim([freq_low_limit freq_high_limit]);
ylim([0 1]);
xlabel('Frequency (Hz)','FontSize',16);
ylabel('Absorption Coefficient','FontSize',16);
set(gca,'FontSize',14);
grid on;
saveas(gcf,'acoeff_low.fig');
print('acoeff', '-dpng', '-r600');
```

3.png

Figure 6.3: Two-mic transfer function MATLAB code part 3.

References

[1] L. Cremer. Akustische Beihefte. *Acustica*, 3(2):249–263, 1953.

[2] A. D. Lapin. Sound attenuation in waveguides (Review). *Soviet Physics Acoustics*, 21:337–350, 1975.

[3] Philip M. Morse. The transmission of sound inside pipes. *J. Acoust. Soc. Am.*, 11(2):205–210, October 1939.

[4] Philip M. Morse. Acoustic Impedance and Sound Absorption. *J. Acoust. Soc. Am.*, 12(2):217–227, August 1940.

[5] E. L. Shenderov. Eigenfunctions of a planar impedance waveguide. *Acoust. Phys.*, 45(5):589–586, 1999.

[6] E. L. Shenderov. Helmholtz equation solutions corresponding to multiple roots of the dispersion equation for a waveguide with impedance walls. *Acoust. Phys.*, 46(3):357–363, May 2000.

[7] B. J. Tester. The Optimization of Modal Sound Attenuation in Ducts, in the Absence of Mean Flow. *Journal of Sound and Vibration*, 27(4):477–513, January 1973.

[8] Heidi Leni Ruiz Villamil, Pedro Cobo, Thomas Dupont, and Philippe Leclaire. Acoustic properties of perforated plates and screens. In *Societe Francaise d'Acoustique. Acoustics 2012, April 2012, Nantes, France.*, 2012.

[9] Iljae Lee. *Acoustic characteristics of perforated dissipative and hybrid structures.* PhD thesis, Ohio State University, 2005.

[10] Ahmet Selamet, Iljae Lee and Norman T. Huff. Acoustic impedance of perforations in contact with fibrous material. *J. Acoust. Soc. Am.*, 119(5):2785–2797, May 2006.

[11] Joseph W. Sullivan and Malcolm J. Crocker. Analysis of concentric-tube resonators having unpartitioned cavities. *J. Acoust. Soc. Am.*, 1978.

[12] Gang Wu, Shen Li, He Zhao, Xinglin Yang, and Jiaqiang E. Experimental and frequency-domain study of acoustic damping of single-layer perforated plates. *Aerosp. Sci. Technol.*, 2017.

[13] Daniel Paul Warren. *The scattering of sound waves in two-dimensional ducts with discontinuities in height and material property.* PhD thesis, Brunnel University, 1999.

[14] Daniel Potente. General Design Principles of an Automotive Muffler. *ACOUSTICS 2005*, 154–158, November 2005.

[15] Dah-You Maa. A General Reactance Theorem for Electrical, Mechanical, and Acoustical Systems. *I.R.E.*, 365–371, July 1943.

[16] ASTM E1050-98. Standard Test Method for Impedance and Absorption of Acoustical Materials Using a Tube, Two Microphones and A Digital Frequency Analysis System. *American Society for Testing and Materials.*

[17] Sayyajeet P. Deshpande, Mohan D. Rao, Kolano and Saha Engineers, Inc.. Development of a Low Cost Impedance Tube to Measure Acoustic Absorption and Transmission Loss of Materials. *American Society for Engineering Education*, 2014.

[18] Hideo Utsuno, Toshimitsu Tanaka, Takeshi Fujikawa, and A. F. Seybert. Transfer Function Method for Measuring Characteristic Impedance and Propagation Constant of Porous Materials. *J. Acoust. Soc. Am.*, 86(2):637–643, August 1989.

[19] Philip M. Morse and K. Uno Ingard. Theoretical Acoustics. *Mcgraw-Hill*.

[20] David T. Blackstock. Fundamentals of Physical Acoustics. *John Wiley Sons, inc.*

[21] Lawrence E. Kinsler and Austin R. Frey. Fundamentals of Acoustics. *John Wiley Sons, inc.*

[22] Julius S. Bendat and Allan G, Piersol. Engineering Applications of Correlation and Spectral Analysis. *John Wiley Sons, inc.*